

Dipolar ordering transitions in many-body quantum optics: Analytical diagrammatic approach to equilibrium quantum spins

Benedikt Schneider,^{1, 2} Ruben Burkard,³ Beatriz Olmos,³ Igor Lesanovsky,^{4, 5} and Björn Sbierski³

¹Department of Physics and Arnold Sommerfeld Center for Theoretical Physics, Ludwig-Maximilians-Universität München, Theresienstr. 37, 80333 Munich, Germany

²Munich Center for Quantum Science and Technology (MCQST), 80799 Munich, Germany

³*Institut für Theoretische Physik, Universität Tübingen,
Auf der Morgenstelle 14, 72076 Tübingen, Germany*

⁴*Institut für Theoretische Physik and Center for Integrated Quantum Science and Technology, Universität Tübingen, Auf der Morgenstelle 14, 72076 Tübingen, Germany*

⁵School of Physics and Astronomy and Centre for the Mathematics and Theoretical Physics of Quantum Non-Equilibrium Systems, The University of Nottingham, Nottingham NG7 2RD, United Kingdom
(Dated: July 26, 2024)

(Dated: July 20, 2024)

Quantum spin models with a large number of interactions per spin are frequently encountered in modern many-body quantum optical systems like arrays of Rydberg atoms, atom-cavity systems or trapped ion crystals. For theoretical analysis the mean-field (MF) approximation is routinely applied. However, except in the exotic case of infinite connectivity, its results are not quantitatively reliable. Here we present a systematic correction to MF theory based on diagrammatic perturbation theory for quantum spin correlators in thermal equilibrium. Our analytic results are universally applicable for any lattice geometry and spin-length S . We provide pre-computed and easy-to-use building blocks for Ising, Heisenberg and transverse field Ising models in the the symmetry-unbroken regime. We showcase the methods quality and simplicity by computing magnetic phase boundaries and excitations gaps. We also treat the Dicke-Ising model of ground-state superradiance where we show that corrections to the MF phase boundary vanish.

I. INTRODUCTION

The past decade has witnessed tremendous progress at the intersection points of cold atomic physics, quantum optics and many-body physics. Atoms and ions can be confined in spatially structured arrangements [1–4] and brought into interaction using tailored potentials or cavity-mediated forces [5–7]. This has opened a new window for the exploration of equilibrium and non-equilibrium phenomena, including phase transitions in arrays of trapped Rydberg atoms [8] and Wigner crystals of trapped ions [9, 10], super- and subradiance in dense atomic gases [11, 12] or exotic time-crystal phases in atom-cavity systems [13, 14].

One commonality of these quantum optical platforms is that their essential physics is often captured by many-body models whose microscopic degrees of freedom are quantum spins. Such systems are traditionally studied in the context of condensed matter physics. However, the structure of the underlying spin-spin couplings is strikingly different to the short-range interactions encountered in solid-state based quantum magnetism [15]. This is due to long-wavelength photons and phonons that mediate the interactions between atoms and ions, which thereby give rise to tunable long-range and even all-to-all spin-spin couplings [16–20], see Fig. 1.

In this theoretical work we are concerned with the treatment of such highly-connected spin Hamiltonians, motivated but not limited to the above-discussed quantum optical many-body models. Concretely, we will consider general lattice spin- S Hamiltonians with bi-linear

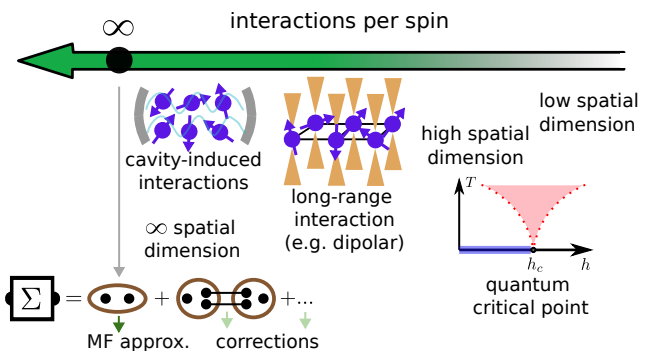


Figure 1. The validity of the MF approximation for magnetic ordering transitions in spin systems depends on the number of interactions per spin (green arrow) and is only exact in the limit of infinite connectivity. Corrections to MF can be moderate in systems if the connectivity of spins is large, a common situation in many-body quantum optics, but also in high spatial dimensions or at quantum critical points. In this regime the diagrammatic method proposed in this work provides accurate results at negligible computational cost.

couplings, that is,

$$H = -h \sum_i S_i^z + \sum_{i < i'} \sum_{\gamma, \gamma' \in \{+, -, z\}} J_{ii'}^{\gamma\gamma'} S_i^\gamma S_{i'}^{\gamma'}, \quad (1)$$

where S_i^γ represents, for the i -th spin, its component along the z -direction and the spin ladder operators for $\gamma = z$ and $\gamma = +, -$, respectively. Moreover, $J_{ii}^{\gamma\gamma'}$ are the coupling constants between spins at lattice sites i

and i' , which may be anisotropic in the spin components and which, in cold atomic experiments, can be controlled by geometry and choice of electronic states. Finally, the field h may be generated and controlled, for example, by laser-induced level shifts.

Our goal is to investigate the properties of the equilibrium state of these models. We assume this state to be thermal and characterized in general by a finite temperature $T \geq 0$, see e.g. Ref. [21] for thermometry of a Rydberg-array [22]. This is certainly an approximation for quantum optical spin systems, which are well-isolated from the environment (in the sense that they are not embedded in a solid-state matrix). Nevertheless, when preparing ground states and also excited states there is a residual entropy, manifesting in fluctuations, albeit not necessarily thermal.

One recurrent quest in this field is to obtain phase diagrams which can be probed in experiment, e.g. in Rydberg tweezer arrays [22]. More recently, also dynamic quantities such as excitation spectra have come into reach [23]. Theoretically, these and other observables can be obtained from two-point spin correlators, see Eq. (7). For example, (second order) phase transitions are signaled by a divergence of the static contribution to the correlator [24]. However, the large number of interaction partners per spin often cause considerable difficulties on the computational side: The plain high-temperature expansion of static correlators [25] becomes ineffective (see however Ref. [26]), and approaches relying on finite simulation volumes, e.g., density matrix renormalization group (DMRG) and quantum Monte Carlo (QMC), often suffer from finite-size effects. Furthermore, these methods may be negatively affected by high dimensionality ($d > 1$) or the sign-problem [24].

As a complementary method, the mean-field (MF) approximation is routinely applied. It amounts to approximating the full Hamiltonian (1) by a non-interacting trial Hamiltonian with variational parameters chosen to optimize the free energy [27] (see also Ref. [28] for an insightful discussion). This procedure is often cut short by applying the mnemonically intuitive replacement

$$S_i^\gamma S_{i'}^{\gamma'} \rightarrow S_i^\gamma \langle S_{i'}^{\gamma'} \rangle + \langle S_i^\gamma \rangle S_{i'}^{\gamma'} - \langle S_i^\gamma \rangle \langle S_{i'}^{\gamma'} \rangle \quad (2)$$

to the interaction term in Hamiltonian (1), followed by a self-consistent determination of $\langle S_i^\gamma \rangle$.

In the limit of infinite connectivity, the MF approximation is quantitatively exact [29, 30]. Examples are all-to-all interactions (e.g. cavity mediated in the limit of an infinite number of spins [31, 32]) or the limit of infinite dimension. However, more realistic Hamiltonians feature a large but finite connectivity, so that the MF approximation is expected to be quantitatively inaccurate but qualitatively correct [33]. This regime which, as argued above, is naturally realized in many quantum optical spin systems, is the main focus of this work. We show that the spin-spin correlator and the derived observables, including phase boundaries or excitation gaps, can be well approximated by a simple and computationally

inexpensive spin-diagrammatic approach that rests on an expansion in powers of a suitably defined small parameter which varies from one problem to another. Importantly, we show that our approach also works at $T = 0$ where at quantum critical points the (effective) dimensionality is increased [34].

The foundations of the diagrammatic technique for quantum spins were laid in the late 1960s [35–40]. In Sec. II, we review the basic idea of the method and introduce a novel and efficient way to evaluate the diagrams to unprecedented order. Staying in the symmetry unbroken regime, in Sec. III we provide explicit expressions for the two-point functions of general $h = 0$ Heisenberg models and the Ising and transverse-field Ising model (TFIM), the latter at $T = 0$. In Sec. IV we benchmark our method using various toy models on the hypercubic-lattice with nearest-neighbor interactions. Finally, in Sec. V, we apply our method to two particular quantum optical many-body systems with $S = 1/2$, both on the square lattice: A power-law interacting ferromagnetic (FM) Heisenberg model at $T > 0$ [41] and the Dicke-Ising model at $T = 0$ [42, 43]. We conclude in Sec. VI.

II. DIAGRAMMATIC TECHNIQUE FOR QUANTUM SPINS VIA KERNEL FUNCTIONS

A. Models and perturbative expansion

We consider SU(2) quantum spin- S operators $\mathbf{S}_j = (S_j^x, S_j^y, S_j^z)^T$ on a lattice with N sites labeled by index j . The operators obey the spin algebra

$$[S_{j_1}^{\alpha_1}, S_{j_2}^{\alpha_2}] = i\delta_{j_1 j_2} \epsilon^{\alpha_1 \alpha_2 \alpha_3} S_{j_1}^{\alpha_3} \quad (3)$$

with $\alpha_{1,2,3} \in \{x, y, z\}$ and the operator spin-length constraint $\mathbf{S}_j \cdot \mathbf{S}_j = S(S+1)$. The Hamiltonian is given in Eq. (1) where $S^\pm = (S^x \pm iS^y)/\sqrt{2}$ are the spin rising and lowering operators. In the following, it is understood that $\alpha \in \{x, y, z\}$ while $\gamma \in \{+, -, z\}$.

The following three choices for h and $J_{ii'}^{\gamma\gamma'}$ correspond to standard spin models that we consider in this work: (i) The Ising model

$$H = \sum_{i < i'} J_{ii'} S_i^z S_{i'}^z \quad (4)$$

is obtained from Eq. (1) by setting $h = 0$ and $J_{ii'}^{\gamma\gamma'} = \delta_{\gamma,z} \delta_{\gamma',z} J_{ii'}$. (ii) The transverse field Ising model (TFIM)

$$H = \sum_{i < i'} J_{ii'} S_i^x S_{i'}^x - h \sum_i S_i^z \quad (5)$$

corresponds to $J_{ii'}^{\gamma\gamma'} = \frac{1}{2} (1 - \delta_{\gamma,z}) (1 - \delta_{\gamma',z}) J_{ii'}$. Note that Ising models are usually defined for $S = 1/2$. (iii) The Heisenberg model

$$H = \sum_{i < i'} J_{ii'} \mathbf{S}_i \cdot \mathbf{S}_{i'} \quad (6)$$

results from $h = 0$ and $J_{ii'}^{\gamma\gamma'} = \delta_{\bar{\gamma},\gamma'} J_{ii'}$ where we define $\bar{\gamma}$ by $\bar{-} = -$, $\bar{+} = +$ and $\bar{z} = z$. As mentioned above, we keep S general but assume vanishing onsite-coupling $J_{ii} = 0$ for simplicity.

In the remainder of this work, we focus on the Matsubara spin-spin correlation function,

$$G_{jj'}^{\alpha\alpha}(i\nu_m) = T \int_0^\beta d\tau d\tau' e^{i\nu_m(\tau-\tau')} G_{jj'}^{\alpha\alpha}(\tau, \tau'), \quad (7)$$

where τ is (imaginary) time, $\beta = 1/T$ is the inverse temperature, $\nu_m = 2\pi T m$ with $m \in \mathbb{Z}$ a (bosonic) Matsubara frequency and

$$G_{jj'}^{\alpha\alpha}(\tau, \tau') = G_{jj'}^{\alpha\alpha}(\tau - \tau') = \langle \mathcal{T}S_j^\alpha(\tau)S_{j'}^\alpha(\tau') \rangle \quad (8)$$

the time-ordered (“ \mathcal{T} ”) thermal correlation function [40] which only depends on the time difference. Time ordering for spin operators is defined via

$$\mathcal{T}S_j^\alpha(\tau)S_{j'}^{\alpha'}(\tau') = \begin{cases} S_j^\alpha(\tau)S_{j'}^{\alpha'}(\tau') & : \tau > \tau', \\ S_{j'}^{\alpha'}(\tau')S_j^\alpha(\tau) & : \tau' > \tau, \end{cases} \quad (9)$$

and operators in imaginary-time Heisenberg picture are denoted as $S_j^\alpha(\tau) \equiv e^{H\tau} S_j^\alpha e^{-H\tau}$. Thermal averages are defined as $\langle \dots \rangle = \mathcal{Z}^{-1} \text{Tr} [e^{-\beta H} \dots]$ where $\mathcal{Z} = \text{Tr} e^{-\beta H}$ is the partition function.

While dynamic observables are encoded in the analytically continued version of Eq. (7), $G_{jj'}^{\alpha\alpha}(i\nu_m \rightarrow \nu \pm i\eta)$, we will be mainly concerned with the detection of magnetic phase transitions of second-order (continuous) nature. Such a transition towards an ordered phase (with $\langle S_i^\alpha \rangle \neq 0$, say) can be conveniently detected coming from the paramagnetic side without spontaneous symmetry breaking, see the black arrow in Fig. 2(a). According to isothermal linear response theory, it is signaled by a divergent spatial Fourier transform (at ordering wavevector \mathbf{Q}) of the static Matsubara spin-spin correlator [Eq. (7) with $\nu_m = 0$] also known as spin susceptibility [24]. Note that around first-order (discontinuous) transitions, where the order parameter jumps, the susceptibility is not defined. The analysis of first-order transition is beyond the scope of this work.

Next, we review the diagrammatic series expansion of $G_{jj'}^{\alpha\alpha}(i\nu_m)$ in J , originally developed for the case of quantum spins in Refs. [35–39] and summarized in Ref. [40]. Earlier work on the (classical) Ising model can be found in Refs. [29, 44, 45]. As usual in perturbation theory [27], we start by splitting the Hamiltonian in interacting and non-interacting parts. For the general spin Hamiltonian (1), we thus set $H = H_{0,h} - V$ where

$$H_{0,h} = -h \sum_i S_i^z, \quad V = - \sum_{i < i'} \sum_{\gamma, \gamma' \in \{+, -, z\}} J_{ii'}^{\gamma\gamma'} S_i^\gamma S_{i'}^{\gamma'}. \quad (10)$$

The formal series expansion in $V \sim J$ reads [27]

$$\begin{aligned} G_{jj'}^{\gamma\gamma'}(\tau, \tau') &= \sum_{n=0}^{\infty} \frac{1}{n!} \int_0^\beta d\tau_1 \dots d\tau_n \\ &\times \langle \mathcal{T}V(\tau_1) \dots V(\tau_n) S_j^\gamma(\tau) S_{j'}^{\gamma'}(\tau') \rangle_{0,h,V-c}. \end{aligned} \quad (11)$$

Here, the averages and Heisenberg evolution of operators is only with respect to $H_{0,h}$ (we avoid a new symbol since no confusion is possible from here on). For G , we changed to flavor indices $\gamma, \gamma' \in \{+, -, z\}$ adapted to the U(1) symmetry of $H_{0,h}$. This will prove convenient below. The subscript $V-c$ for the averages on the right-hand side of Eq. (11) excludes vacuum diagrams [27] where one or more $V(\tau)$ are not connected to the external indices after performing the average. We refer to App. A for a definition. Note that a formula analogous to Eq. (11) applies for any time-ordered product of Heisenberg-picture operators and in particular also for the local magnetization $\langle \mathcal{T}S_j^\alpha(\tau) \rangle = \langle S_j^\alpha \rangle$. However, in this work we will focus on two-point functions.

Finally we perform the τ, τ' -integral of Eq. (11) to obtain the Matsubara correlator (7) and specialize to a fixed expansion order n indicated by a superscript,

$$\begin{aligned} G_{jj'}^{\gamma\gamma'(n)}(i\nu_m) &= T \frac{1}{n!} \int_0^\beta e^{i\nu_m(\tau-\tau')} d\tau_1 \dots d\tau_n d\tau d\tau' \quad (12) \\ &\times \langle \mathcal{T}V(\tau_1) \dots V(\tau_n) S_j^\gamma(\tau) S_{j'}^{\gamma'}(\tau') \rangle_{0,h,V-c}. \end{aligned}$$

B. Diagrams, J-reducibility and MF approximation

We proceed with the evaluation of Eq. (12) by a diagrammatic formulation [40]. The diagrammatic approach is conceptually simple, physically transparent and allows for various subsequent approximation and resummation schemes one of which will be essential later. In the following, we review the diagrammatic method, the concept of J-reducibility and its relation to the MF approximation (2). In the next subsection, we will propose a novel evaluation scheme of the diagrams that provides analytical expressions at high orders J^n .

The diagrammatic formulation starts from the graphical representation of Eq. (11) in Fig. 2(b). The dots represent spin operators and for now we do not perform the Fourier transform to Matsubara frequency. The two external spin operators carry multi-indices $1 = (\gamma, j, \tau)$ and $2 = (\gamma', j', \tau')$. All other (internal) spin operators coming from V appear pairwise connected by interaction lines representing $-J_{i_k i'_k}$, $k = 1, 2, \dots, n$. Flavors, times and sites of the internal spin operators are summed (or integrated) over and the leading factor $1/n!$ is shown explicitly. Note that interaction lines connect spin operators at the same time (unless they are retarded, c.f. Sec. V B).

Next, the V -connected free spin average in Eq. (11) is taken by co-localizing the $2n + 2$ spin operators (dots) in any possible way involving blocks of $m = 1, 2, 3, 4, \dots$ spins shown as brown ellipses, see Fig. 2(c) [40]. These blocks represent connected equal-site time ordered free spin correlators,

$$\langle \mathcal{T}S_i^{\gamma_1}(\tau_1) \dots S_i^{\gamma_m}(\tau_m) \rangle_{0,c,h} = G_{0,c,h}^{\gamma_1 \dots \gamma_m}(\tau_1, \dots, \tau_m), \quad (13)$$

which, for the homogeneous non-interacting Hamiltonian $H_{0,h}$ that we consider in Eq. (10), do not depend on the

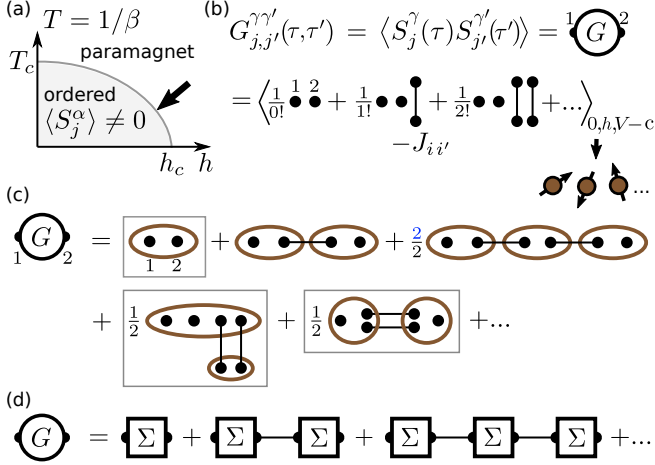


Figure 2. (a) Schematic of a typical phase diagram for Hamiltonian (1). In this work we approach the magnetic ordering transition from the paramagnetic phase. (b) Diagrammatic representation of the expansion for the spin-spin correlator G in the exchange interaction $-J$ (lines), the orders $n = 0, 1, 2$ are shown explicitly. (c) Diagrammatic representation of the V -connected correlators in (b) in terms of ordinary connected free-spin correlators (brown ellipses). The 1-J-irreducible diagrams are marked with boxes, their sum constitutes the 1-J-irreducible part Σ of G . (d) The Larkin equation re-combines Σ and J to form G .

site index i . Connected spin correlators (with subscript c) are defined in analogy to their V -connected counterparts, see App. A. Due to our choice of $J_{ii} = 0$, interaction lines cannot start and end at the same block. In Fig. 2(c), the absence of blocks of size $m = 1$ representing single-spin averages (magnetization) is due to our current focus on the paramagnetic regime. The presence of blocks of order $m > 2$ signals the absence of Wick's theorem [27] for spin operators, ultimately rooted in the operator-valued right-hand side of the commutation relation (3) which differs from the canonical case of bosonic creation and annihilation operators.

An important special case for Eq. (13) occurs if all m flavor indices are chosen as z such that all the corresponding operators $S_i^z(\tau_n) = S_i^z$ commute. These connected z -spin correlators are then time-independent and given via the order- $(m-1)$ derivative of the Brillouin function $b_c(y)$ which describes the magnetization of a free spin $\langle S^z \rangle$ dependent on $y = \beta h$ [40],

$$G_{0,c,h}^{z,z}(\tau_1, \dots, \tau_m) = b_c^{(m-1)}(\beta h), \quad (14)$$

$$b_c(y) = (S + \frac{1}{2}) \coth \left[(S + \frac{1}{2})y \right] - \frac{1}{2} \coth \frac{y}{2}. \quad (15)$$

For $h \rightarrow 0$ we abbreviate $b_c^{(m-1)}(0) \equiv b_{c,m-1}$, e.g. $b_{c,1} = S(S+1)/3$ is the free spin (static) Curie susceptibility that will become important in the following discussion. Note that for $h = 0$ all single-spin blocks [Eq. (13) with $m = 1$] vanish.

Having explained the building blocks of the diagrams in Fig. 2(c), we now turn their topology, i.e. the particular choice of blocks and their connection. Topological multiplicity factors Λ (denoted in blue) appear if the same diagram topology can be arrived at distributing the dots in Fig. 2(b) to the given set of blocks in multiple ways, see e.g. the last diagram in the first line of Fig. 2(c). Diagrams that only differ by a rearrangement of dots *within* blocks are not topologically different. Formally, the multiplicity factor can be computed via the number of elements in the automorphism group \mathcal{A}_g of a diagram g of order J^n : $\Lambda = n!/\text{ord}(\mathcal{A}_g)$.

The diagrams in Fig. 2(c) can be classified as either 1-J reducible or 1-J irreducible (1JI). In 1-J reducible diagrams, it is possible to separate the external spin operators (single dots) by cutting a single interaction line. If this is not the case, the diagram is 1JI. The symbol Σ denotes the infinite sum of all 1JI diagrams. For examples, the contributions to Σ of order J^0 and J^2 are indicated with boxes in Fig. 2(c).

All diagrammatic contributions to the spin correlator that are 1-J reducible can be represented by 1JI diagrams connected by one or more interaction lines, see Fig. 2(d). This diagrammatic expression can be summed exactly and yields the Larkin equation [35, 40]. In frequency space, it reads

$$G(i\nu_m) = (1 + \Sigma(i\nu_m) \cdot J)^{-1} \cdot \Sigma(i\nu_m). \quad (16)$$

Here all objects are considered $N \times N$ matrices with two site indices, c.f. Eq. (7) and for our purposes the flavors will all be set to a fixed α with $\alpha \in \{x, y, z\}$ for simplicity. Note the similarity of Eq. (16) to Dyson's equation for canonical bosonic or fermionic systems [27] which however rests on the concept of cutting free propagator (and not interaction) lines.

Given the above diagrammatic rules, it is straightforward to write down the 1JI diagrams for Σ at order n indicated by $\Sigma^{(n)}$. The diagrams for $n \leq 3$ which include the boxed diagrams of Fig. 2(b) are shown in Fig. 3. We label the different diagram topologies at order n with an additional index $x = a, b, c, \dots$. Each diagram topology is uniquely identified by (nx) . The diagrams for $\Sigma^{(4)}$ have not been systematically collected so far in literature and are given in Fig. 7 of App. D.

We conclude this subsection by linking the diagrammatic expansion to the MF approximation for $G^{\alpha\alpha}$. The latter is obtained by using only the lowest-order approximation for Σ (see the arrow in Fig. 3)

$$\Sigma^{\alpha\alpha} \rightarrow \Sigma^{\alpha\alpha(0)} = G_{0,c,h}^{\alpha\alpha}. \quad (17)$$

For $\alpha = z$, this evaluates to $b_c^{(1)}(\beta h)$, see Eq. (14). We also assumed $\langle S_i^\alpha \rangle = 0$, otherwise h in Eq. (17) would need to be replaced by the Weiss field, see Ref. [40] and Sec. V B. The easiest way to see the correspondence between Eq. (17) and the MF approximation is to recall that the latter is exact for $N \rightarrow \infty$ if each spin interacts with all other spins in the system via $J \rightarrow J/N$.

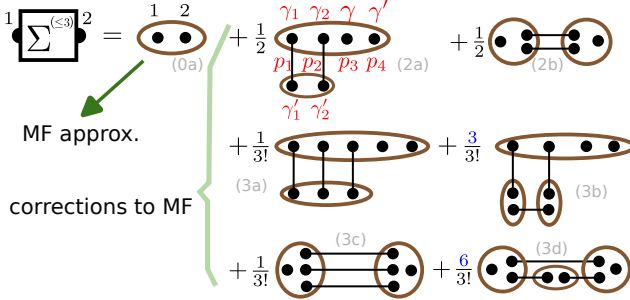


Figure 3. Diagrams for Σ up to order J^3 for a situation where single-spin expectation values are not involved. The blue multiplicity factors $\Lambda^{(nx)}$ denote the number of ways to arrive at a given diagram starting from the expansion in Fig. 2(b), e.g. in diagram (3b) there are three choices to pick the bottom line from the three lines available at third order perturbation theory. The two vertical lines are equivalent and do not enhance the multiplicity as an exchange can be compensated by a permutation of sites within the top brown ellipse.

For G , this means that string-like diagrams as in the first line of Fig. 2(c) are the only finite contribution for $N \rightarrow \infty$. This follows since the site-indices of the internal (2-)blocks can roam freely over all available sites only in string-like diagrams while being more restricted in diagrams that contain loops. Finally, the string-like diagrams are exactly the diagrams that are produced by the replacement $\Sigma \rightarrow \Sigma^{(0)}$ in the Larkin equation of Fig. 2(d). It follows that corrections of order $n > 0$ to Σ represent corrections to the MF results, see Figs. 1 and 3.

C. Diagram evaluation via kernel functions

The remaining task is to calculate the analytical expressions encoded in the particular diagrams $\Sigma_{jj'}^{(nx)}(i\nu_m)$ representing the different contributions of the right-hand side of Eq. (12). As the values for the blocks [brown ellipses, see Eq. (13)] are site-independent and we specialize to only a single type of spin-spin interaction J in Eq. (1) (e.g. no XXZ interactions), we can pull out all $J_{ii'}$ stemming from the insertions of V [c.f. Eq.(10)] with the remaining free site sums,

$$\Sigma_{jj'}^{(nx)}(i\nu_m) \equiv t_{jj'}^{(nx)}[J] \cdot \sigma^{(nx)}(i\nu_m). \quad (18)$$

This geometry factor $t_{jj'}^{(nx)}[J] \sim J^n$ completely captures the dependence of the particular diagram (nx) on j, j' and the underlying $N \times N$ coupling matrix $J_{ii'}$. For example, with regard to Fig. 3, the geometry factor for diagram (0a) is simply $\delta_{jj'}$ whereas for (2a) and (2b) we read off

$$t_{jj'}^{(2a)} = \delta_{jj'} \sum_i J_{ji} J_{ij}, \quad t_{jj'}^{(2b)} = (J_{jj'})^2. \quad (19)$$

The geometry factors for all diagrams of order $n = 0, 2, 3$ are shown in the second column in Tab. I. In the third col-

top.	r-space $t_{jj'}^{(nx)}$	k-space $t_{\mathbf{k}}^{(nx)}$	nn-hyp. $\tilde{t}_{\mathbf{k}}^{(nx)}$
(0a)	$\delta_{jj'}$	1	1
(2a)	$\delta_{jj'} [J \cdot J]_{jj'}$	$\int_{\mathbf{q}} J_{\mathbf{q}}^2$	$J_1 \tilde{J}_0$
(2b)	$J_{jj'}^2$	$\int_{\mathbf{q}} J_{\mathbf{q}-\mathbf{k}} J_{\mathbf{q}}$	$J_1 \tilde{J}_{\mathbf{k}}$
(3a)	$\delta_{jj'} \sum_i J_{ji}^3$	$\int_{\mathbf{p}, \mathbf{q}} J_{\mathbf{p}} J_{\mathbf{q}} J_{\mathbf{p}+\mathbf{q}}$	$J_1^2 \tilde{J}_0$
(3b)	$\delta_{jj'} [J \cdot J \cdot J]_{jj'}$	$\int_{\mathbf{q}} J_{\mathbf{q}}^3$	0
(3c)	$J_{jj'}^3$	$\int_{\mathbf{q}, \mathbf{p}} J_{\mathbf{p}-\mathbf{k}} J_{\mathbf{q}} J_{\mathbf{p}+\mathbf{q}}$	$J_1^2 \tilde{J}_{\mathbf{k}}$
(3d)	$J_{jj'} [J \cdot J]_{jj'}$	$\int_{\mathbf{q}} J_{\mathbf{k}-\mathbf{q}} J_{\mathbf{q}}^2$	0

Table I. Geometry factors $t^{(nx)}[J]$ for Σ -diagrams of order $n = 0, 2, 3$ and all topologies (for the case $n = 4$ see Tab. VI). Results in the second column are given in real space [where $J_{jj'}^2$ is understood as $(J_{jj'})^2$ etc.]. The third column shows the same results in momentum space (where we abbreviate $\int_{\mathbf{q}} = 1/N \sum_{\mathbf{q}}$). In the fourth column, momentum space results are specialized for an infinite d -dimensional hypercubic lattice with a lattice constant of unity and nearest-neighbor coupling J_1 where $\tilde{J}_{\mathbf{k}} \equiv 2J_1 \sum_{\mu=1}^d \cos k_{\mu}$ and accordingly $\tilde{J}_0 = 2dJ_1$.

umn, we provide the momentum space representation for translation invariant lattices with spatial Fourier transform defined by

$$\mathbf{J}_{\mathbf{k}} = \sum_{\mathbf{r}_j} e^{-i\mathbf{k} \cdot \mathbf{r}_j} J_{0, \mathbf{r}_j}, \quad (20)$$

and analogous for $G_{\mathbf{k}}$ and $\Sigma_{\mathbf{k}}$. In the fourth column we specialize to the infinite ($N \rightarrow \infty$) nearest-neighbor hypercubic lattice model in d spatial dimensions, see the caption of Tab. I for more details. Geometry factors for the fourth-order diagrams $\Sigma^{(4)}$ are summarized in Tab. VI of App. D.

Beyond the geometry factor, the remaining contribution in Eq. (18) denoted as $\sigma^{(nx)}$ only depends on the type of spin model (here: Heisenberg, Ising, TFIM) and includes the topological multiplicity factor $\Lambda^{(nx)}$ of the diagram (nx) . In principle, obtaining $\sigma^{(nx)}$ is straightforward in frequency space [40] where interaction lines proportional to $\delta_{\nu_m + \nu'_m}$ connect the blocks which are temporal Fourier transforms of Eq. (13), $G_{0,c,h}^{\gamma_1 \dots \gamma_m}(\omega_1, \dots, \omega_{m-1})$. The latter, however, are difficult to calculate in general beyond the z -only case (14), especially for $h = 0$ where a distinction of cases regarding various frequency combinations is required. Despite recent algorithmic advances [46, 47] the general $G_{0,c,h}^{\gamma_1 \dots \gamma_m}(\omega_1, \dots, \omega_{m-1})$ (which beyond their appearance in perturbation theory lack physical significance for large m) are currently known analytically up to order $m = 4$ [40], which would only suffice to compute Σ to order $n = m - 2 = 2$. On the other hand, without the temporal Fourier transform and for a fixed order of times, the blocks representing $\langle \mathcal{T} S^{\gamma_1}(\tau_1) \dots S^{\gamma_m}(\tau_m) \rangle_{0,c,h}$ [c.f. Eq. (13)] simplify to standard free-spin equal-time averages $\langle S^{\gamma_1} \dots S^{\gamma_m} \rangle_{0,c,h}$ which can be efficiently computed for general S , see Sec. 6.2. in Ref. [47].

Here, the crucial insight is that it is possible to reformulate $\sigma^{(nx)}$ such that only the simple free-spin equal-time correlators $\langle S^{\gamma_1} \dots S^{\gamma_m} \rangle_{0,c,h}$ are required. As derived

in App. B, all the remaining complexity is encapsulated in the universal kernel functions $K_{n+2}(\Omega_1, \dots, \Omega_{n+2})$ of Ref. [47]. The latter originally appeared in the context of Fourier transforms of time-ordered correlation functions. The connection is based on the interpretation of an n -th order perturbative expression as a Fourier transform of a time-ordered correlation function of order $n+2$

with n frequencies set to zero.

The translation of diagram (nx) to an expression $\sigma^{(nx)}$ is straightforward. To avoid unnecessary complicated notation, we just give two examples: With the red labeling of interaction lines and flavors in Fig. 3, diagram (2a) yields

$$\begin{aligned} \sigma^{\gamma\gamma'(2a)}(i\nu_m) &= \Lambda^{(2a)} \frac{(-1)^n}{n!} \sum_{\gamma_{1,\dots,n}^{(r)}} \sum_{p \in S_{n+2}} K_{n+2}(\mathcal{P}\{\Omega_1(p_1), \dots, \Omega_{n+2}(p_{n+2})\}) \\ &\times \left\langle \mathcal{P}S^{\gamma_1}(p_1)S^{\gamma_2}(p_2)S^{\gamma}(p_3)S^{\gamma'}(p_4) \right\rangle_{0,c,h} \left\langle \mathcal{P}S^{\gamma'_1}(p_1)S^{\gamma'_2}(p_2) \right\rangle_{0,c,h}, \end{aligned} \quad (21)$$

where $\Lambda^{(2a)} = 1$ and $n = 2$. As another example, diagram (3b) with $\Lambda^{(3b)} = 3$ and $n = 3$ is

$$\begin{aligned} \sigma^{\gamma\gamma'(3b)}(i\nu_m) &= \Lambda^{(3b)} \frac{(-1)^n}{n!} \sum_{\gamma_{1,\dots,n}^{(r)}} \sum_{p \in S_{n+2}} K_{n+2}(\mathcal{P}\{\Omega_1(p_1), \dots, \Omega_{n+2}(p_{n+2})\}) \\ &\times \left\langle \mathcal{P}S^{\gamma_1}(p_1)S^{\gamma_2}(p_2)S^{\gamma}(p_4)S^{\gamma'}(p_5) \right\rangle_{0,c,h} \left\langle \mathcal{P}S^{\gamma'_1}(p_1)S^{\gamma_3}(p_3) \right\rangle_{0,c,h} \left\langle \mathcal{P}S^{\gamma'_2}(p_2)S^{\gamma'_3}(p_3) \right\rangle_{0,c,h}. \end{aligned} \quad (22)$$

The internal flavor sums over $\gamma_{1,\dots,n}^{(r)}$ depend on the model, e.g. for the Heisenberg case these sums are over $\{+, -, z\}$ while restricted to $\{z\}$ in the Ising case. The second sum is over the $(n+2)!$ permutations S_{n+2} that determine the ordering of the argument list of K_{n+2} and the spin operators in the equal-time averages. This is accomplished by the index ordering operator \mathcal{P} . This operator applies to operator strings and argument lists alike. It acts like time-ordering, but for discrete indices $(1), (2), \dots, (n+2)$ that - unlike imaginary time arguments - do not affect the operator, for example $\mathcal{P}S^+(1)S^-(3)S^z(2) = S^-S^zS^+$. Finally, the Ω -list is given by

$$\{\Omega_1, \dots, \Omega_n, \Omega_{n+1}, \Omega_{n+2}\} = \{-(\gamma_1 + \gamma'_1)h, \dots, -(\gamma_n + \gamma'_n)h, i\nu_m - \gamma h, -i\nu_m - \gamma' h\}, \quad (23)$$

where the following replacement rule for flavor labels is understood: $\{z, +, -\} \rightarrow \{0, +1, -1\}$.

A closed-form expressions for general kernel functions $K_k(\Omega_1, \dots, \Omega_k)$ can be found in Ref. [47]. The expressions grow in complexity with k , however, for this work with the specific form of the Ω -list in Eq. (23) and our focus on either $h = 0$ (Ising and Heisenberg models) or $T \rightarrow 0$ (for the TFIM), the kernel functions can be simplified considerably. The resulting expressions are given in App. C.

Expressions analogous to Eqns. (21) and (22) can be straightforwardly written for all diagrams and can be evaluated via computer algebra. In the next section, we provide the expressions for $\sigma^{\gamma\gamma'(nx)}(i\nu_m)$ obtained in this way. These should be summed up to find the full $\Sigma^{(n)}$ at order J^n ,

$$\Sigma_{jj'}^{\gamma\gamma'(n)}(i\nu_m) = \sum_{x=a,b,c,\dots} t_{jj'}^{(nx)} [J] \sigma^{\gamma\gamma'(nx)}(i\nu_m). \quad (24)$$

III. ANALYTIC RESULTS FOR 1-J IRREDUCIBLE DIAGRAMS

In this section we report the analytic results of the diagram evaluation up to third order in J for the Ising model, TFIM at $T = 0$ and the Heisenberg model as defined in Eqns. (4), (5) and (6). Diagrams in fourth order and their analytic results are relegated to App. D. In the diagrams, single-spin blocks representing $\langle S_i^\alpha \rangle$ are not required. This is evident in the paramagnetic phase of the Ising and Heisenberg model where these quantities vanish. For the symmetry-unbroken phase of the TFIM they are finite for $\alpha = z$ but these blocks do not appear in the expansion of $G^{xx} = \text{Re}[G^{++} + G^{+-}]$.

We provide results for the second contribution to Eq. (18), the geometry independent $\sigma^{\gamma\gamma'(nx)}(i\nu_m)$. For the Ising model and TFIM case we consider σ^{zz} and σ^{xx} , respectively, see Tab. II. In both cases diagrams which involve blocks of any odd order vanish and are not listed. For the Ising model this is due to spin flip symmetry $S_i^z \rightarrow -S_i^z \forall i$ in the paramagnetic phase, for the σ^{xx} in the TFIM this follows from the fact that the blocks are solely made from S^+ and S^- which need to appear in equal numbers for any finite contribution in light of U(1)

	Ising $T^{1+n}\sigma^{zz(nx)}(i\nu_m = 0)$	TFIM $\sigma^{xx(nx)}(i\nu) _{T=0}$
(0a)	$b_{c,1}$	$\frac{hS}{h^2+\nu^2}$
(2a)	$\frac{1}{2}b_{c,1}b_{c,3}$	$\frac{-S^2(5h^2+\nu^2)}{16h(h^2+\nu^2)^2}$
(3b)	$\frac{-1}{2}b_{c,1}^2b_{c,3}$	$\frac{S^3(4h^2+\nu^2)}{16h^2(h^2+\nu^2)^2}$
(3c)	$\frac{-1}{6}b_{c,3}^2$	$\frac{-S^2}{16(h^2+\nu^2)^2}$

Table II. Ising model and TFIM at $T = 0$, both in the paramagnetic phase: Expansion of the lattice independent parts $\sigma^{(nx)}$ of the diagrams $\Sigma^{(nx)}$ for $n = 0, 2, 3$ for all non-zero topologies, c.f. Eq. (18). The derivatives of the Brillouin function (15) at zero field are denoted by $b_c^{(m)}(0) \equiv b_{c,m}$. Fourth order results are given in Tab. VII.

spin rotation symmetry of $H_{0,h}$. For the Ising model only static contributions are finite due to its classical nature.

The results for $\Sigma_{jj'}^{\gamma\gamma'(n)}(i\nu_m)$ computed by summing over topologies [Eq. (24)] have been tested for small clusters of spins, e.g. for the dimer with $N = 2$ and $J_{12} = J_{21} = J_1$ and $J_{11} = J_{22} = 0$. In this case, for moderately large S , the Hilbert space is small and the exact two-point function G can be found using the spectral representation [27]. Hence the exact Σ is obtained via Eq. (16). This exact result can then be expanded in J_1 and compared against $\Sigma_{jj'}^{\gamma\gamma'(n)}(i\nu_m)$ computed diagrammatically. As an example, for the TFIM dimer with $J_1 > 0$, $T = 0$ and $S = 1/2$, one confirms

$$\Sigma_{11}^{xx}(i\nu) = \frac{h}{2(h^2+\nu^2)} - J_1^2 \frac{5h^2+\nu^2}{64h(h^2+\nu^2)^2} + J_1^4 \frac{(43h^4+14h^2\nu^2+3\nu^4)}{4096h^3(h^2+\nu^2)^3} + O(J_1^6), \quad (25)$$

$$\Sigma_{12}^{xx}(i\nu) = J_1^3 \frac{-1}{64h(h^2+\nu^2)^2} + O(J_1^5). \quad (26)$$

As some diagrams like (3b) vanish for the dimer geometry it is important to also check the fully connected trimer with $N = 3$ in an analogous fashion.

Finally, we turn to the Heisenberg case at $T > 0$ where the $\sigma^{zz(nx)} = \sigma^{\alpha\alpha(nx)}$ are reported in Tab. III. We need to distinguish between the static case $\nu_m = 0$ and the dynamic case $\nu_m = 2\pi m T \neq 0$ for which we abbreviate $\Delta = \frac{1}{2\pi m}$. Again, these results have been tested for small spin clusters. A further non-trivial check for the resulting $\Sigma^{(n)}$ is the fulfillment of the property $\Sigma_{\mathbf{k}=0}^{(n)}(i\nu_m \neq 0) = 0$ following from the fact that $S_{\mathbf{k}=0}^z$ is a constant of motion in a Heisenberg system.

IV. HYPERCUBIC LATTICE BENCHMARKS

We now proceed to test the applicability of the diagrammatic expansion for nearest-neighbor models on the hypercubic lattice in d spatial dimensions with AFM coupling $J_1 > 0$. The geometry factors and further details

	$T^{1+n}\sigma^{zz(nx)}$	static ($\nu_m = 0$)	dyn. ($\nu_m \neq 0$)
(0a)	$b_{c,1}$	0	
(2a)	$\frac{b_{c,1}^2}{-6}$ $(1 + 6b_{c,1})$	$+2\Delta^2 b_{c,1}^2$	
(2b)	$\frac{b_{c,1}^2}{-12}$	$-2\Delta^2 b_{c,1}^2$	
(3a)	$\frac{b_{c,1}^2}{-24}$ $(1 + 4b_{c,1})$	$+\frac{1}{2}\Delta^2 b_{c,1}^2$	
(3b)	$\frac{b_{c,1}^3}{8}$ $(1 + 6b_{c,1})$	$-2\Delta^2 b_{c,1}^3$	
(3c)	$\frac{b_{c,1}^2}{-120}$ $(48b_{c,1}^2 + 16b_{c,1} + 3)$	$-\frac{1}{2}\Delta^2 b_{c,1}^2$	
(3d)	0	$+2\Delta^2 b_{c,1}^3$	

Table III. Heisenberg model at $T > 0$ in the paramagnetic phase: Expansion of the lattice independent parts $\sigma^{(nx)}$ of the diagrams $\Sigma^{(nx)}$ for $n = 0, 2, 3$, c.f. Eq. (18). Fourth order results are given in Tab. VII. The Δ in the dynamic case stands for $1/(2\pi m)$.

on the lattice can be found in Tab. I. For the Ising and Heisenberg case we focus on the magnetic ordering temperature T_c and for the TFIM at $T = 0$ we consider the critical field h_c and the excitation gap $\Delta(h)$. The latter serves as an example for a dynamical quantity which needs to be evaluated via analytical continuation.

The magnetic phase boundary is signaled by the divergence of the static susceptibility, according to Eq. (16),

$$G_{\mathbf{k}}^{-1}(i\nu_m = 0) = 1/\Sigma_{\mathbf{k}}(i\nu_m = 0) + J_{\mathbf{k}} \stackrel{!}{=} 0, \quad (27)$$

with \mathbf{k} replaced by the Néel wavevector $\mathbf{N} = (\pi, \pi, \dots, \pi)$. Thus the critical coupling is given by the solution of $0 \stackrel{!}{=} 1/\Sigma_{\mathbf{N}} - 2dJ_1$. We specialize to the thermal transition in the Ising case (with $S = 1/2$) or Heisenberg case. First, as stated before, the MF approximation for T_c is found by replacing $\Sigma_{\mathbf{N}} \rightarrow \Sigma_{\mathbf{N}}^{(0)} = \beta b_{c,1}$ in the above equation which yields the well-known MF result $T_c^{(0)} = 2d b_{c,1} J_1 \sim d$. We then divide Eq. (27) by T and proceed to obtain corrections to the MF result for T_c . We thus seek a consistent expansion of

$$1/(T\Sigma_{\mathbf{N}}) = 2d\beta J_1 \quad (28)$$

in the small parameter $1/d \ll 1$ where MF is approximately valid so that $X_1 \equiv \beta J_1$ close to criticality is of order $\sim 1/d$. With this in mind we provide the hyper-cubic geometry factors $\beta^n \tilde{t}_{\mathbf{k}=\mathbf{N}}^{(nx)}$ for all non-vanishing topologies in Tab. IV. Next to the diagram label we show the leading scaling with $1/d$ of the particular $\beta^n \tilde{t}_{\mathbf{k}=\mathbf{N}}^{(nx)}$ close to the thermal transition which does depend both on order n and topology x . We can thus expand $1/(T\Sigma_{\mathbf{N}})$ up to order $(1/d)^m$, drop all higher orders and solve numerically for T_c . Since the $\Sigma^{(n)}$ are available up to $n = 4$, we

$(0a) \sim d^0$	$(2a) \sim d^{-1}$	$(2b) \sim d^{-1}$	$(3a) \sim d^{-2}$	$(3c) \sim d^{-2}$
1	$+2dX_1^2$	$-2dX_1^2$	$+2dX_1^3$	$-2dX_1^3$
$(4a) \sim d^{-3}$	$(4b) \sim d^{-2}$	$(4c) \sim d^{-3}$	$(4e) \sim d^{-2}$	$(4f) \sim d^{-2}$
$+2dX_1^4$	$+4d^2X_1^4$	$-2dX_1^4$	$-8d^2X_1^4$	$+4d^2X_1^4$
$(4h) \sim d^{-2}$	$(4j) \sim d^{-2}$	$(4l) \sim d^{-2}$	$(4m) \sim d^{-2}$	
$+4d^2X_1^4$	$6d[2d-1]X_1^4$	$6d[2d-1]X_1^4$	$-6d[2d-1]X_1^4$	

Table IV. Non-vanishing geometry factors $\beta^n \tilde{t}_{\mathbf{k}=\mathbf{N}}^{(nx)} [J]$ ($n \leq 4$) for the nearest-neighbor d -dimensional hyper-cubic lattice with coupling J_1 as a function of $X_1 = \beta J_1$. The leading-order scaling in powers of $1/d$ close to the thermal ordering transition is provided next to the diagram label. Geometry factors for $n > 4$ (not shown) are of order d^{-3} or smaller.

d	exact	$O(1/d)$	$O(1/d^2)$	spin-fRG [51]	spin-DMFT [52]
3	0.752	0.789	0.740	0.744	0.659
4	0.835	0.854	0.839	0.839	0.807
5	0.878	0.887	0.880	0.880	0.865
6	0.903	0.908	0.904	0.904	
7	0.919	0.923	0.920	0.920	

Table V. Ising model: Critical temperature $T_c/T_c^{(0)}$ for the d -dimensional nearest-neighbor Ising model ($S = 1/2$) on the hypercubic lattice normalized to the MF transition temperature $T_c^{(0)} = d|J_1|/2$. The quasi-exact benchmark results in the second column [48–50] are compared to the results obtained from Eq. (29) evaluated up to order $1/d$ and $1/d^2$, respectively. For comparison, the last two columns provide results from spin-fRG [51] and spin-DMFT [52].

can consider $m = 0, 1, 2$, c.f. Tab. IV. Explicitly, we have

$$\frac{1}{T\Sigma_{\mathbf{N}}} = \frac{1}{T\sigma^{(0)}} - \frac{A_1}{(T\sigma^{(0)})^2} + \frac{A_2}{(T\sigma^{(0)})^3} + O(d^{-3}), \quad (29)$$

$$A_1 = 2dX_1^2 T^3 \left(\sigma^{(2a)} - \sigma^{(2b)} \right), \quad (30)$$

$$\begin{aligned} A_2 = A_1^2 - T^4 \sigma^{(0)} [2dX_1^3 \left(\sigma^{(3a)} - \sigma^{(3c)} \right) \\ + 4d^2 X_1^4 T (\sigma^{(4b)} - 2\sigma^{(4e)} + \sigma^{(4f)} + \sigma^{(4h)} \\ + 3\sigma^{(4j)} + 3\sigma^{(4l)} - 3\sigma^{(4m)})], \end{aligned} \quad (31)$$

where $A_1 \sim 1/d$ and $A_2 \sim 1/d^2$.

For the Ising case, we report the results for the so obtained $T_c/T_c^{(0)}$ and $d = 3, 4, 5, 6, 7$ in Tab. V. The quasi-exact results from high-order series expansion or Monte Carlo simulations [48–50] are rapidly approached as the order m in $1/d$ is increased, showing the validity of our expansion even down to $d = 3$. We also compare our results at order $1/d^2$ to other diagrammatic approaches with different resummation strategies: Our results are similar to the spin functional RG approach (spin-fRG) by Krieg and Kopietz [51], only at $d = 3$ the latter has a slight advantage. The dynamical MF theory for spins [52] (spin-DMFT) is not competitive. This is not surprising given DMFT's local approximation of Σ already fails in order J^3 where the non-local diagram (3c) appears [53].

For the Heisenberg model, benchmark checks of T_c suffer from the scarcity of exact results for $d > 3$. The exception is the classical case ($S \rightarrow \infty$) for $d = 4$. Here

$T_c/T_c^{(0)}$ improves from 0.8536 in order $1/d$ to 0.8315 in order $1/d^2$ with the exact result at 0.822 [54]. For the case $d = 3$ and $S < \infty$, Eq. (28) often yields non-real solutions at the limited expansion orders available. An exception is the case $d = 3$, $S = 3/2$ for which $T_c/T_c^{(0)}$ improves from 0.769 in order $1/d$ to 0.657 in order $1/d^2$ towards the exact result at 0.702 [55].

For the TFIM at $T = 0$, the critical field at the ordering transition is given from Eq. (27) as

$$1/(d\Sigma_{\mathbf{N}}^{xx}) \stackrel{!}{=} 2J_1. \quad (32)$$

The MF approximation with $\Sigma_{\mathbf{N}}^{xx} \rightarrow S/h$ yields $h_c^{(0)} = 2dSJ_1 \sim d$. Using $\sigma^{xx(n)}(i\nu = 0)|_{T=0} \sim 1/h^{1+n}$ we again expand the left-hand side for $h \gtrsim h_c$ in orders of $1/d$ which yields expressions similar to Eq. (29). We focus on the case $d = 3$, $S = 1/2$ and report the results for h_c in Fig. 4, see vertical lines. The exact Monte Carlo result $h_c^{(MC)} = 2.57907(3)J_1$ [56] is rapidly approached.

To showcase the advantage of analytical expressions for the Matsubara correlator, we consider the excitation gap Δ for $h \gtrsim h_c$ which we obtain from the dynamical xx -spin correlator, $G_{\mathbf{k}}^{xx}(i\nu \neq 0)$. The latter also contains the dispersion of spin waves transversal to the magnetization in the S^z direction. The dispersion $\omega_{\mathbf{k}}$ is determined by the position of the sharp peak in $\text{Im}G_{\mathbf{k}}^{xx,R}(\nu)$. For $h \rightarrow h_c$ from above, we expect $\omega_{\mathbf{k}}$ to vanish at $\mathbf{k} = \mathbf{N}$ where the spin wave softens and order sets in. For $h > h_c$, the gap is thus defined as $\Delta = \omega_{\mathbf{N}}$ and we consider

$$G_{\mathbf{N}}^{xx}(i\nu) = \frac{1/d}{\frac{1}{d\Sigma_{\mathbf{N}}^{xx}(i\nu)} - 2J_1}. \quad (33)$$

We use an expansion of the denominator similar to above which we here evaluate to order $1/d$ (and analogously for MF and order $1/d^2$). We find

$$G_{\mathbf{N}}^{xx}(i\nu) \simeq \frac{hS}{h^2 + \frac{5}{8}dSJ_1^2 - 2dShJ_1 - (i\nu)^2 \left(1 + \frac{dSJ_1^2}{8h^2} \right)} \quad (34)$$

and after analytic continuation the gap is obtained as

$$\Delta^{(1/d)} = \sqrt{(h^2 - 2dShJ_1 + \frac{5}{8}dSJ_1^2)/(1 + \frac{dSJ_1^2}{8h^2})}. \quad (35)$$

Setting $d = 3$ and $S = 1/2$, this agrees very well with recent iPEPS tensor network simulations in Ref. [57], see Fig. 4 (blue dashed line and dots). For $h \gtrsim h_c$, the iPEPS is actually closer to $\Delta^{(1/d)}$ than to $\Delta^{(1/d^2)}$ which we suspect to be an artifact of finite bond dimension.

V. APPLICATION TO MODELS FROM MANY-BODY QUANTUM OPTICS

A. Long-range square lattice Heisenberg model

As a first of two applications inspired from many-body quantum optical systems we consider the $S = 1/2$ Heisenberg square lattice model with long-range FM power law

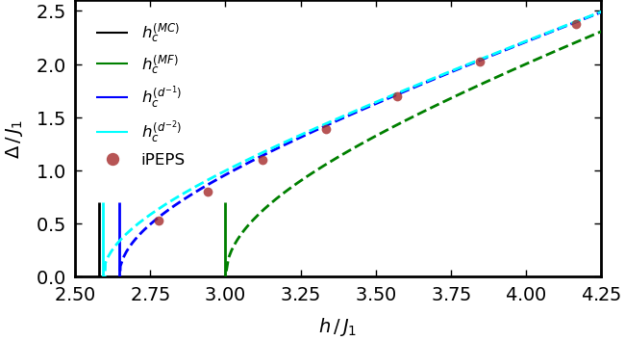


Figure 4. TFIM on the cubic lattice at $T = 0$ and $S = 1/2$. The vertical lines indicate the critical field h_c , the exact result [56] (black) is rapidly approached by the $1/d$ expansion of the left-hand side of Eq. (32). The same expansion is also used to estimate the spectral gap Δ shown by dashed lines. The first correction to MF approximation is already in good agreement to the tensor-network (iPEPS) simulation of Ref. [57].

interactions,

$$J_{ii'} = J_1 / |\mathbf{r}_i - \mathbf{r}_{i'}|^\alpha, \quad (36)$$

with $J_1 < 0$. This model has been recently studied with QMC simulations [41] numerically expensive due to the large system sizes required to approximate the infinite system limit. The lattice constant is set to unity and the interesting regime for the power-law exponent is $\alpha \in (2, 4)$ [58]. In this range α is large enough for a well-defined thermodynamic limit but small enough to allow a finite FM ordering temperature $T_c > 0$ by evading the Mermin-Wagner theorem [59]. We abbreviate $J_{\mathbf{r}_j} = J_1 / |\mathbf{r}_j|^\alpha$.

In analogy to Sec. IV, T_c is determined from

$$-\beta J_{\mathbf{k}=\mathbf{0}} = 1 / (T \Sigma_{\mathbf{k}=\mathbf{0}}). \quad (37)$$

To compute the spatial Fourier transform $J_{\mathbf{k}=\mathbf{0}}$ on the left-hand side and for subsequent expansions on the right-hand side, we obtain numerically the lattice sums $I^{(m)} \equiv \sum_j r_j^{-\alpha m}$ for $m = 1, 2, 3$. Then $J_{\mathbf{k}=\mathbf{0}} = J_1 I^{(1)}$. To identify a suitable expansion scheme, we consider the integral approximation of $I^{(m)}$ with lower bound $a = O(1)$,

$$I^{(m)} \simeq \int_a^\infty dr r^{1-\alpha m} = \frac{a^{2-m\alpha}}{m\alpha-2} \xrightarrow{\alpha \rightarrow 2} \begin{cases} \sim \frac{1}{\alpha-2} & : m = 1, \\ \text{const.} & : m > 1. \end{cases} \quad (38)$$

For $\alpha \rightarrow 2$ from above, $I^{(m)}$ only diverges for $m = 1$ whereas it is finite for $m > 1$.

From Eq. (37) the MF critical temperature is

$$T_c^{(0)} = |J_1| b_{c,1} I^{(1)} \sim \frac{1}{\alpha-2}, \quad (39)$$

see the green line in Fig. 5. We use $\alpha - 2$ as the small parameter for the expansion on the right-hand side of Eq. (37). We consider the geometry factors $\beta^n t_{\mathbf{k}=\mathbf{0}}^{(nx)}$ that

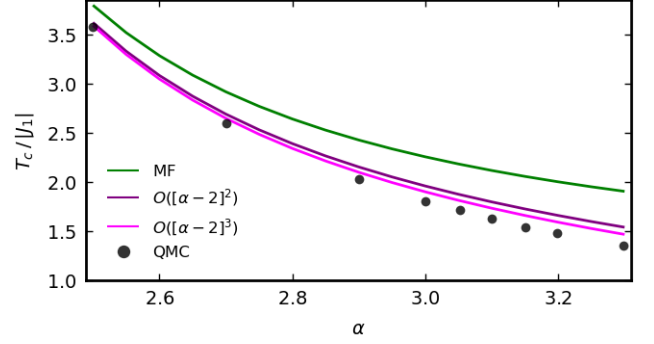


Figure 5. Ordering temperature for the $S = 1/2$ square lattice Heisenberg FM with couplings decaying as a power law with exponent α , see Eq. (36). Dots denote reference data from QMC taken from Ref. [41]. Colored lines indicate T_c in MF approximation (green), and adding corrections up to order $[\alpha - 2]^2$ (purple) and $[\alpha - 2]^3$ (magenta), respectively.

play a role for the static Heisenberg case and we limit ourselves to order $n \leq 3$. For diagram (3b), we numerically checked that $\sum_{i,j} J_{\mathbf{r}_j} J_{\mathbf{r}_i - \mathbf{r}_j} J_{\mathbf{r}_i} \equiv J_1^3 \tilde{I}^{(3)}$ is non-singular for $\alpha \rightarrow 2$, this then means that $T \Sigma^{(n)} \sim \beta^n \sim [\alpha - 2]^n$ around criticality. We use this insight to expand the right-hand side in Eq. (37) to third order in $\alpha - 2$ and obtain

$$\begin{aligned} & b_{c,1} \beta |J_1| I^{(1)} = 1 \\ & - b_{c,1}^{-1} (\beta |J_1|)^2 I^{(2)} T^3 \left(\sigma^{(2a)} + \sigma^{(2b)} \right) \\ & + b_{c,1}^{-1} (\beta |J_1|)^3 T^4 \left[I^{(3)} \left(\sigma^{(3a)} + \sigma^{(3c)} \right) + \tilde{I}^{(3)} \sigma^{(3b)} \right] + \dots \end{aligned} \quad (40)$$

The results for $S = 1/2$ are shown in Fig. 5 and approach the QMC data quickly if $\alpha - 2$ is sufficiently small.

B. Dicke-Ising model: Ground-state superradiance

As a second application to a many-body quantum optical system we consider the Dicke-Ising model [42, 43, 60, 61]. This also provides an example where single-spin blocks appear in the diagrammatic expansion. Also note that the pre-computed diagrams of Sec. III will not be used in the following exact calculation.

The Hamiltonian features a competition between a homogeneous field $h > 0$ in z -direction, a coupling of the total spin- x to a cavity photon and a nearest-neighbor AFM Ising zz -interaction V , see Fig. 6(a) for a sketch. The Hamiltonian is given by $H = H_x + H_z$ with

$$H_x = \omega a^\dagger a + \frac{g}{\sqrt{N}} (a + a^\dagger) \sum_i S_i^x, \quad (41)$$

$$H_z = -h \sum_i S_i^z + \frac{V}{2} \sum_{\langle i, i' \rangle} \left(S_i^z + \frac{1}{2} \right) \left(S_{i'}^z + \frac{1}{2} \right) \quad (42)$$

$$= -[h - V] \sum_i S_i^z + \frac{V}{2} \sum_{\langle i, i' \rangle} S_i^z S_{i'}^z. \quad (43)$$

Here, the cavity photon at frequency ω is created by a^\dagger . The sums go over N sites and the nearest neighbor bonds, respectively. The cavity-dipole coupling is $g/\sqrt{N} > 0$. This ensures an extensive interacting energy in the infinite system limit $N \rightarrow \infty$ which we consider in the following. For concreteness, we specialize to a square lattice geometry. However, our qualitative results below do not depend on this choice.

The Dicke model (the case $V = 0$) and its phase transition to the symmetry-broken superradiant state (the FM state with $\langle S_i^x \rangle \neq 0$) has been studied thoroughly both in theory [17, 31] and experiment [62], the latter in a non-equilibrium setting. However, comparatively little is known about the Dicke-Ising model ($V > 0$) [42, 43, 60, 61] which is yet awaiting experimental implementation. A possible realization for the Ising zz -interactions uses the concept of Rydberg dressing [63] which motivated the form of Eq. (42) and leads to a renormalized effective field $h \rightarrow h - V$ when rewritten as in Eq. (43).

So far, the model also contains bosonic degrees of freedom in variance to the spin-only formulation in Hamiltonian (1). However, assuming a thermal state we can trace out the photons on the level of the generating functional [64]. This replaces H_x by an all-to-all retarded (i.e. frequency dependent) FM spin interaction of the xx -type,

$$H_x \rightarrow H_{x,ret} = T \sum_{\nu_m} \frac{1}{2} \sum_{i,i'} S_i^x(-\nu_m) J_{ii'}^{xx}(\nu_m) S_{i'}^x(\nu_m), \quad (44)$$

with $J_{ii'}^{xx}(\nu_m) = -2g^2\omega/[N(\nu_m^2 + \omega^2)]$. This is close to Eq. (1), only differing in the frequency dependence and the presence of an onsite term. As we will discuss, this is inconsequential in the following since no xx -interactions will appear in the 1JI diagrammatic expansion.

Here, we focus on thermal equilibrium at $T \rightarrow 0$ and limit the investigation to the realistic case of small V ($V \ll h$) and its effect on the transition between the z -polarized and superradiant phase. For $V \rightarrow 0$, it is well known that the MF approximation is exact for the Dicke model [17] but what happens at $V > 0$? As a first step, in Ref. [42] the phase boundary for the Dicke-Ising model on the square lattice was determined in MF approximation,

$$g_c = \sqrt{\omega(h - 2V)}, \quad (45)$$

see Fig. 6(b) for a sketch.

Two questions are in order: First, is the phase transition indeed continuous as in MF approximation? And second, if yes, what are the corrections to the phase boundary from MF approximation?

As shown in Ref. [61] for a simplified and more symmetric version of the Dicke-Ising model with $h - V = 0$ (with no z -polarized phase), the transition between the superradiant and Ising phase is of first order in a chain geometry. However, it is currently unknown if and under which conditions this also holds for the more realistic case $V \ll h$ and the phase transition out of the fully polarized phase that we consider.

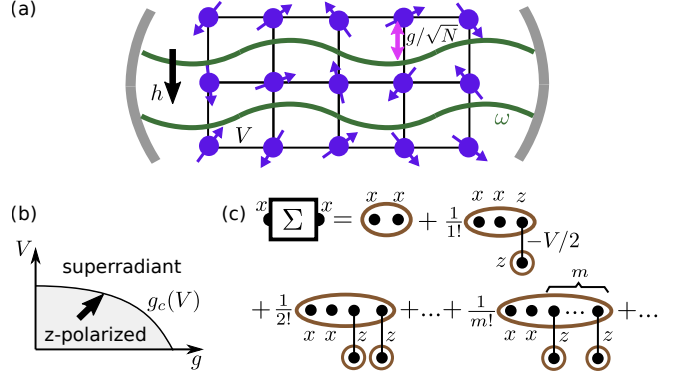


Figure 6. Dicke-Ising model: (a) Sketch of an experimental square lattice setup with cavity photons at frequency ω coupled to spins with strength g/\sqrt{N} , homogeneous z -field h and nearest-neighbor AFM Ising interactions V induced via Rydberg dressing. (b) Schematic phase diagram in the vicinity of the z -polarized phase and the adjacent superradiant phase in the presence of AFM Ising interactions V . (c) Diagrammatic expansion for Σ^{xx} in the limit $N \rightarrow \infty$ and $T \rightarrow 0$ can be summed exactly. This shows that the exact phase boundary in (b) is described by the MF result Eq. (45).

Making the assumption that the phase transition from the z -polarized to the superradiant phase is continuous (and can thus be detected via a divergence in spin-susceptibility) we use the spin diagrammatic technique to show rigorously our main finding of this section: Eq. (45) is already the exact result. This conclusion has been obtained independently in the very recent work of Schellenberger and Schmidt [43] using an alternative algebraic approach.

Analogous to the other examples in this paper, we start from the z -polarized symmetry-unbroken phase and approach the boundary of the superradiant phase, see the arrow in Fig. 6(b). We detect the critical light-matter coupling strength g_c from the divergence of the static FM correlator $G_{\mathbf{k}=\mathbf{0}}^{xx}(i\nu = 0)$,

$$1/\Sigma_{\mathbf{k}=\mathbf{0}}^{xx} + J_{\mathbf{k}=\mathbf{0}}^{xx} \stackrel{!}{=} 0 \quad (46)$$

Here and in the following we drop the zero-Matsubara frequency argument from all quantities. The static part of the retarded xx -interaction (44) is $J_{\mathbf{k}=\mathbf{0}}^{xx} = -2g^2/(\omega N)$ and Σ^{xx} denotes the J^{xx} -irreducible part of G^{xx} . Next, we expand Σ^{xx} in J^{xx} and V with the non-interacting Hamiltonian being $H_{0,h-V} = -[h - V] \sum_i S_i^z$. The first observation is that due to the limit $N \rightarrow \infty$ any occurrence of an interaction $J_{ii'}^{xx} \sim 1/N$ needs to be accompanied with a free site summation. Since these diagrams are necessarily J^{xx} -reducible (c.f. the discussion at the end of Sec. II B) they do not occur in Σ^{xx} and only the V -interactions $\sim S_i^z S_{i'}^z$ need to be considered. The second observation pertains to z -only blocks $G_{0,c,h-V}^{zz}(\tau_1, \dots, \tau_k) = b_c^{(k-1)}(\beta[h - V])$. In the limit $T \rightarrow 0$ where the spins are fully polarized, these generalized susceptibilities vanish except for $k = 1$ for which

$$G_{0,c,h-V}^z(\tau_1) = S = 1/2.$$

These considerations equate the exact (and local) Σ^{xx} to the infinite sum of diagrams shown in Fig. 6(c). The calculation proceeds without the kernel trick or any pre-computed diagrams of Sec. III since all diagrammatic objects are free of frequency loops and are to be evaluated only at zero frequency where they are easy to obtain. We only need $\Sigma^{xx(0)} = 1/(2[h - V])$, see Tab. II for the TFIM. The fully static mixed-flavor blocks with two S^x operators and m appearances of the S^z operator can be found via a k -fold derivative of $G_{0,c,h-V}^{xx}$ with respect to h (which thus is also used as a source field),

$$\overbrace{G_{0,c,h-V}^{xxz...z}}^m = \partial_h^k G_{0,c,h-V}^{xx} = \frac{(-1)^m m!}{2[h - V]^{m+1}}. \quad (47)$$

With these preparations the infinite diagrammatic sum in Fig. 6(c) results in the *exact* expression

$$\begin{aligned} \Sigma_{\mathbf{k}=0}^{xx} &= \sum_{m=0}^{\infty} \frac{1}{m!} \overbrace{G_{0,c}^{xxz...z}}^m \cdot \langle S^z \rangle_{0,c}^m \cdot \left(-4 \frac{V}{2}\right)^m \quad (48) \\ &= \frac{1}{2(h - 2V)}. \end{aligned}$$

Inserting this in Eq. (46) we obtain that the exact g_c is given by Eq. (45).

For future work on the Dicke-Ising model, an extension to the complete phase diagram which includes also a z -AFM and a combined z -AFM and superradiant x -FM phase, would be interesting. According to Ref. [43], MF theory is again exact for the transition between the latter two phases. Likewise, we suggest to consider the experimentally relevant modifications to finite N and to the experimentally relevant open-system case [65].

VI. CONCLUSION

In summary, we have presented an analytic approach to Matsubara spin-spin correlation functions based on a diagrammatic expansion of their 1-J-irreducible part Σ to n -th order in J . We provide closed-form expressions for $n \leq 4$ for Ising, TFIM and Heisenberg models of completely general lattice geometry and spin length S . The introduction of the kernel function trick was instrumental in this calculation. The final results are conveniently tabulated for forthcoming application in diverse contexts where other computationally much more involved methods like tensor networks or QMC are at their limits or not applicable at all.

Via many examples and by applying a composite expansion strategy involving the inverse dimension (or similar) as a small parameter, we showed the quantitative success of the diagrammatic approach if applied to models qualitatively described by the MF approximation. We argued that this is often the case in highly-connected spin models relevant for state-of-the-art many-body quantum

optical experiments. We use a long-range Heisenberg model and the Dicke-Ising model, both on the square lattice, as a showcase. Moreover we provided various benchmark examples for nearest-neighbor models on the (hyper-)cubic lattice where our method yields accurate magnetic phase boundaries (both at $T > 0$ for Ising and Heisenberg models and $T = 0$ for TFIM). We emphasize that due to the analytic nature of our approach analytic continuation can be easily performed and was shown to lead to competitive results for the gap in the TFIM.

Future work could extend our approach to yet higher orders in J , a greater variety of spin models, including those with multiple spin-spin coupling constants, e.g. XXZ models [66], or with $SU(N)$ symmetry for $N > 2$ [67]. Also, the treatment of the symmetry-broken phase for the study of magnetization and spin-wave properties [46, 68] is within reach. Further, it would be interesting to consider analytic continuation beyond the computation of the gap to obtain spectral functions. These are routinely measured in inelastic neutron scattering on solid-state magnets [69] or, more recently via quench spectroscopy in Rydberg tweezer arrays [23]. For the static case, analytic insights offered by our approach are essential to shed new light [70] onto the puzzle of quantum-to-classical correspondence for static spin correlation functions in $d > 1$ dimensions [71].

Finally, we point out that the combination of the spin-spin correlator's bare series expansion with the kernel function trick [c.f. Eq. (B2)] is suitable for evaluation by a diagrammatic Monte Carlo approach [72]. The latter can be set up similar to the connected determinant algorithm [73], however imaginary time has been already integrated exactly. Implementing these ideas would open the spin diagrammatic method to higher orders and to more flexible resummation schemes beyond this work.

Note added: During the completion of the manuscript, we became aware of independent work in Ref. [74] which computes $\Sigma^{(0,2,3)}$ for the Heisenberg model in the traditional diagrammatic way via frequency integrals. The diagrammatic expansion was derived from an expansion of spin-fRG flow equations. Applications concern estimates of T_c for the $d = 3, 4$ hyper-cubic case for various S . However, due to the chosen expansion of $1/\Sigma$ in J , the quality of the results for T_c does not improve with expansion order, in contrast to the composite expansion strategies presented in this work.

VII. ACKNOWLEDGMENT

We thank Marin Bukov, Elio König, Peter Kopietz, Andreas Rückriegel, Achim Rosch, Johannes Reuther and Sebastian Slama for useful discussions and the authors of Ref. [57] for sharing their iPEPS data. We acknowledge funding from the Deutsche Forschungsgemeinschaft (DFG, German Research Foundation) through the Research Unit FOR 5413/1, Grant No. 465199066. B.Sch. acknowledges funding from the Munich Quantum

Valley, supported by the Bavarian state government with funds from the Hightech Agenda Bayern Plus. B.Sb. and

B.Sch. are supported by DFG grant no. 524270816. I.L. acknowledges financing from the Baden-Württemberg Stiftung through Project No. BWST_ISF2019-23

Appendix A: V-connected correlators

We define the V -connected correlators [27] (subscript $V-c$) that appear in the formal expansion of the spin correlator in Eq. (11) and the following equations. For brevity, we set $S_j^\gamma(\tau)S_{j'}^{\gamma'}(\tau') = A$. Then the V -connected correlators are defined recursively via

$$\langle \mathcal{T}V(\tau_1)\dots V(\tau_n)A \rangle_{0,h,V-c} = \langle \mathcal{T}V(\tau_1)\dots V(\tau_n)A \rangle_{0,h} - \sum_{p \in S_n} \sum_{j=0}^{n-1} \langle \mathcal{T}V(\tau_{p(1)})\dots V(\tau_{p(j)})A \rangle_{0,h,V-c} \langle \mathcal{T}V(\tau_{p(j+1)})\dots V(\tau_{p(n)}) \rangle_{0,h}. \quad (\text{A1})$$

Here S_n denotes the set of permutations of the imaginary time labels $\{1, 2, \dots, n\}$. Standard connected spin correlators [with subscript c first appearing in Eq. (13)] are defined in analogy to their V -connected counterparts in Eq. (A1) by replacing each $V(\tau_j)$ with a single spin operator and removing the external operators $A \rightarrow 1$.

Appendix B: Evaluation of $\sigma^{\gamma\gamma'(nx)}(i\nu_m)$ via kernel function trick

To facilitate all calculations on the right-hand side of Eq. (12) and in particular the evaluation of $\sigma^{(nx)}$ we introduce what we call the kernel function trick. Originally, kernel functions have been introduced to link the Fourier transform of (imaginary) time-ordered m -point correlation functions $G_{A_1\dots A_m}(i\omega_1, \dots, i\omega_{m-1})$ to eigenstates and -energies $H|\underline{a}\rangle = E_{\underline{a}}|\underline{a}\rangle$ of a many-body system [75]. The m -point correlators are a generalization of Eq. (7) to m arbitrary operators $A_{1,2,\dots,m}$. For the frequency arguments we introduced an abbreviated notation where ω_1 is short for ω_{n_1} and so on. The kernel functions straightforwardly extend the well-known spectral (or Lehmann) representation of the 2-point correlator [27] to the m -point case. For bosonic (and spin) operators, the spectral representation reads [47]

$$G_{A_1\dots A_m}(i\omega_1, \dots, i\omega_{m-1}) = \frac{1}{Z} \sum_{p \in S_m} \sum_{\underline{1\dots m}} e^{-\beta E_{\underline{1}}} A_{p(1)}^{12} A_{p(2)}^{23} \dots A_{p(m)}^{m1} K_m \left(\Omega_{p(1)}^{12}, \Omega_{p(2)}^{23}, \dots, \Omega_{p(m-1)}^{m-1m} \right), \quad (\text{B1})$$

where $A_k^{ab} = \langle \underline{a}|A_k|\underline{b}\rangle$ are matrix elements and the argument of the kernel function K_m is a list of m complex numbers $\Omega_k^{ab} = i\omega_k + E_{\underline{a}} - E_{\underline{b}}$ which sum to zero so that the last one is often dropped as in Eq. (B1). The kernel functions itself are completely universal and do neither depend on the Hamiltonian H nor on the operators A_k in Eq. (B1). For example, $K_2(\Omega_1) = -\Delta_{\Omega_1} + \beta\delta_{\Omega_1}/2$ where $\delta_x = \delta_{0,x}$ and $\Delta_x = (1 - \delta_x)/x$. The recent advance in Ref. [47] was the calculation of K_m for general m .

In the context of diagram evaluation, the crucial insight is that kernel functions and n -th order perturbative expressions are naturally connected by interpreting the right-hand side of Eq. (12) as a Fourier transform of a time-ordered correlator of order $n+2$ with the first n frequencies being zero. Hence, as the main technical result of this work, Eq. (12) is expressed as

$$\begin{aligned} G_{jj'}^{(\gamma\gamma')^{(n)}}(i\nu_m) &= \frac{(-1)^n}{n!} \sum_{p \in S_{n+2}} \sum_{i_1 < i'_1, \dots, i_n < i'_n} \sum_{\gamma_1^{(\prime)}, \dots, \gamma_n^{(\prime)} \in \{+, -, z\}} J_{i_1 i'_1}^{\gamma_1 \gamma'_1} \dots J_{i_n i'_n}^{\gamma_n \gamma'_n} \\ &\times \langle B_{p(1)} B_{p(2)} \dots B_{p(n+2)} \rangle_{0,h,V-c} K_{n+2}(\Omega_{p(1)}, \Omega_{p(2)}, \dots, \Omega_{p(n+1)}). \end{aligned} \quad (\text{B2})$$

Here we replaced V using Eq. (10) and defined the following operator and complex frequency lists

$$\{B_1, \dots, B_n, B_{n+1}, B_{n+2}\} = \left\{ S_{i_1}^{\gamma_1} S_{i'_1}^{\gamma'_1}, \dots, S_{i_n}^{\gamma_n} S_{i'_n}^{\gamma'_n}, S_j^\gamma, S_{j'}^{\gamma'} \right\}, \quad (\text{B3})$$

$$\{\Omega_1, \dots, \Omega_n, \Omega_{n+1}, \Omega_{n+2}\} = \{-(\gamma_1 + \gamma'_1)h, \dots, -(\gamma_n + \gamma'_n)h, i\nu_m - \gamma h, -i\nu_m - \gamma' h\}. \quad (\text{B4})$$

Note that the external indices on the left-hand side of Eq. (B2) determine the last two entries of the lists. The Ω -list (B4) was already given in Eq. (23). It is to be understood with the following replacement rule of flavor labels by numbers: $\{z, +, -\} \rightarrow \{0, +1, -1\}$. The simple structure of $H_{0,h}$ with its many-body (product) eigenstates and ladder-like energies is essential in the derivation of Eq. (B2) as it allows to reduce the complexity of the general Eq. (B1)

and condense the sum over eigenstates to the equal-time free spin correlator. This renders the $\Omega_k^{ab} \equiv i\omega_k + E_{\underline{a}} - E_{\underline{b}}$ only dependent on the flavor(s) $\{+, -, z\}$ of the (composite) operator B_k .

We rewrite Eq. (B2) using an index ordering operator \mathcal{P} . This operator applies to operator strings and argument lists alike. It acts like time-ordering, but for discrete indices $(1), (2), \dots, (n+2)$ that - unlike imaginary time arguments - do not affect the operator, for example $\mathcal{P}B_1(1)B_2(3)B_3(2) = B_2B_3B_1$. We also reinstate the redundant last argument $\Omega_{p(n+2)}$ of K_{n+2} . We obtain

$$G_{jj'}^{\gamma\gamma'(n)}(i\nu_m) = \frac{(-1)^n}{n!} \sum_{p \in S_{n+2}} \sum_{i_1 < i'_1, \dots, i_n < i'_n} \sum_{\gamma_{1,\dots,n}^{(i)} \in \{+, -, z\}} J_{i_1 i'_1}^{\gamma_1 \gamma'_1} \dots J_{i_n i'_n}^{\gamma_n \gamma'_n} \times \langle \mathcal{P}B_1(p_1)B_2(p_2)\dots B_{n+2}(p_{n+2}) \rangle_{0,h,V-c} K_{n+2}(\mathcal{P}\{\Omega_1(p_1), \Omega_2(p_2), \dots, \Omega_{n+2}(p_{n+2})\}), \quad (\text{B5})$$

As the operators B_1, B_2, \dots, B_{n+2} and their associated $\Omega_1, \Omega_2, \dots, \Omega_{n+2}$ appear in all possible orderings, this is evidently the same as Eq. (B2).

To calculate $\sigma^{\gamma\gamma'(nx)}(i\nu_m)$ for a particular 1JI diagram (nx) defined by reference site-configuration $\{i_k^{(nx)} < i_k^{(nx)}\}_{k=1,2,\dots,n}$, we specialize the site-sums in Eq. (B5) to this reference configuration and split off the geometry factor $t^{(nx)}[J]$ as explained in Sec. II C. The V-connected average then becomes an ordinary connected equal-time average with respect to $H_{0,h}$ which factorizes according to the blocks of equal sites characteristic for (nx) . Examples for diagrams (2a) and (3b) are provided in Eqns. (21) and (22), respectively.

Appendix C: Special kernel functions for the cases $h = 0$ and $T = 0$

Kernel functions $K_k(\Omega_1, \Omega_2, \dots, \Omega_k)$ for general complex arguments (obeying $\Omega_1 + \dots + \Omega_k = 0$) and arbitrary $k = 2, 3, 4, \dots$ are provided in Ref. [47]. However, in the context of this paper, where kernel functions are applied in the framework of perturbation theory, we have only two potentially non-real entries in the Ω -list (B4) (the ones at the end which contain $\pm i\nu_m$ related to the external operators). More importantly, we limit ourselves to two special cases, (i) the case $h = 0$ for the Ising and Heisenberg model and (ii) the limit $T \rightarrow 0$ for the TFIM. In these cases substantial simplifications arise.

(i) Case $h = 0$: In Eq. (B5), the arguments of K_k are zero except for a possible non-zero pair of frequencies $\pm i\nu_m = \pm 2m\pi Ti$ shuffled to positions $a_{1,2}$ in the list of length $k = n + 2$,

$$\{\Omega_1, \Omega_2, \dots, \Omega_k\} = (0, 0, \dots, 0, \underbrace{i\nu_m}_{\text{pos. } a_1}, 0, \dots, 0, \underbrace{-i\nu_m}_{\text{pos. } a_2}, \underbrace{0, \dots, 0}_{k-a_2}), \quad (\text{C1})$$

where we assume $a_1 < a_2$ without loss of generality (see below). For this situation, we define

$$K_k(\Omega_1, \Omega_2, \dots, \Omega_k) \equiv K_k^{(h=0)}(a_1, a_2, m). \quad (\text{C2})$$

From Ref. [47], we find after some algebra

$$T^{n-1} K_n^{(h=0)}(a_1, a_2, m) = \begin{cases} \frac{1}{n!} & : m = 0, \\ (-1)^{a_2-a_1} \sum_{l=a_2-a_1}^{n-a_1} \frac{[\Delta_{2\pi m i}]^l}{(n-l)!} \binom{l-1}{a_2-a_1-1} & : \text{otherwise,} \end{cases} \quad (\text{C3})$$

where $\Delta_x = 1/x$ for non-zero x and zero otherwise. For the case that $-i\nu_m$ appears first, $a_1 > a_2$, we can flip the sign of m and obtain $K_k(\Omega_1, \Omega_2, \dots, \Omega_k) = K_k^{(h=0)}(a_2, a_1, -m)$.

(ii) Case $T \rightarrow 0$: Here the kernel functions simplify because certain sums are dominated by inverse temperature $\beta \rightarrow \infty$. Any $\beta \delta_{\omega_1+\dots+\omega_l, 0}$ that remains must be interpreted as $\beta \delta_{\omega_1+\dots+\omega_l, 0} \xrightarrow{T \rightarrow 0} 2\pi \delta(\omega_1 + \dots + \omega_l)$, but this does not appear for the particular correlators we compute in this work. To express the resulting $K_k^{(T \rightarrow 0)}(\Omega_1, \dots, \Omega_k)$ we define the list of the partial sums

$$\{\Omega_1, \Omega_1 + \Omega_2, \Omega_1 + \Omega_2 + \Omega_3, \dots, \Omega_1 + \dots + \Omega_{k-1}\} \equiv \{c_1, c_2, \dots, c_{k-1}\}. \quad (\text{C4})$$

The final expression for $K_k^{(T \rightarrow 0)}$ involves all but the l entries of (C4) which are zero,

$$K_k^{(T \rightarrow 0)}(\Omega_1, \dots, \Omega_k) = (-1)^{k+1+l} \frac{\beta^l}{(l+1)!} \prod_{c_m \neq 0} \frac{1}{c_m}. \quad (\text{C5})$$

Appendix D: Diagrams and results for $\Sigma^{(4)}$

In Fig. 7 we provide the diagrams for Σ to order J^4 with geometry factors and $\sigma^{(nx)}$ given in Tabs. VI and VII.

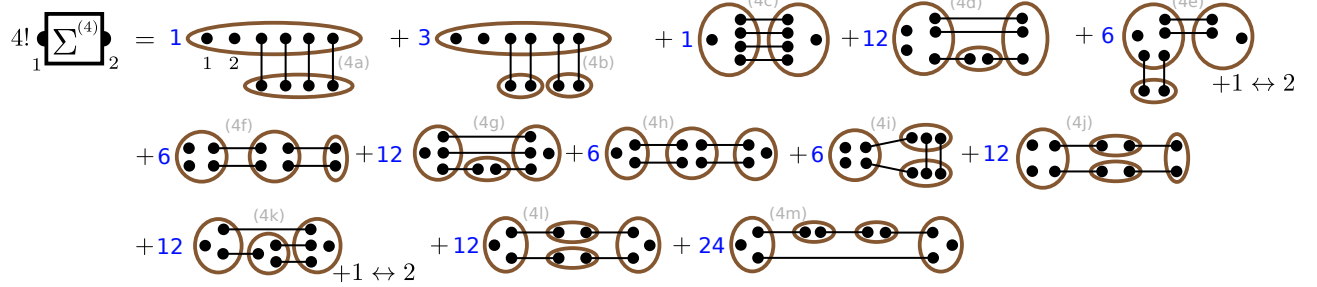


Figure 7. Diagrams for Σ of order J^4 , analogous to Fig. 3. The label $+1 \leftrightarrow 2$ adds the diagram with exchanged external indices.

top.	r-space $t_{jj'}^{(nx)}$	k-space $t_{\mathbf{k}}^{(nx)}$	nn-hyp. $\tilde{t}_{\mathbf{k}}^{(nx)}$
(4a)	$\delta_{jj'} \sum_i J_{ij}^4$	$\int_{\mathbf{p}_{1,2,3}} J_{\mathbf{p}_1} J_{\mathbf{p}_2} J_{\mathbf{p}_3} J_{\mathbf{p}_1 + \mathbf{p}_2 + \mathbf{p}_3}$	$J_1^3 \tilde{J}_0$
(4b)	$\delta_{jj'} [\sum_i J_{ji}^2]^2$	$\left[\int_{\mathbf{q}} J_{\mathbf{q}}^2 \right]^2$	$\left[J_1 \tilde{J}_0 \right]^2$
(4c)	$J_{jj'}^4$	$\int_{\mathbf{p}_{1,2,3}} J_{\mathbf{k} - \mathbf{p}_1} J_{\mathbf{p}_2} J_{\mathbf{p}_3} J_{\mathbf{p}_1 + \mathbf{p}_2 + \mathbf{p}_3}$	$J_1^3 \tilde{J}_{\mathbf{k}}$
(4d)	$\delta_{jj'} \sum_i J_{ji}^2 [J \cdot J]_{ij}$	$\int_{\mathbf{q}, \mathbf{p}} J_{\mathbf{q}} J_{\mathbf{p}} J_{\mathbf{q} + \mathbf{p}}^2$	0
(4e)	$J_{jj'}^2 \sum_i [J_{ji}^2 + J_{ji'}^2]$	$2 \left[\int_{\mathbf{p}} J_{\mathbf{p}}^2 \right] \left[\int_{\mathbf{q}} J_{\mathbf{k} - \mathbf{q}} J_{\mathbf{q}} \right]$	$2 J_1^2 \tilde{J}_0 \tilde{J}_{\mathbf{k}}$
(4f)	$\delta_{jj'} \sum_{i_1, i_2} J_{ji_1}^2 J_{i_1 i_2}^2$	$\left[\int_{\mathbf{q}} J_{\mathbf{q}}^2 \right]^2$	$\left[J_1 \tilde{J}_0 \right]^2$
(4g)	$J_{jj'}^2 [J \cdot J]_{jj'}$	$\int_{\mathbf{q}, \mathbf{p}} J_{\mathbf{k} - \mathbf{p}} J_{\mathbf{p} - \mathbf{q}} J_{\mathbf{q}}^2$	0
(4h)	$[J^2 \cdot J^2]_{jj'}$	$\left[\int_{\mathbf{q}} J_{\mathbf{k} - \mathbf{q}} J_{\mathbf{q}} \right]^2$	$\left[J_1 \tilde{J}_{\mathbf{k}} \right]^2$
(4i)	$\delta_{jj'} [J \cdot J^2 \cdot J]_{jj}$	$\int_{\mathbf{q}} \int_{\mathbf{p}} J_{\mathbf{q}} J_{\mathbf{p}} J_{\mathbf{q} + \mathbf{p}}^2$	0
(4j)	$\delta_{jj'} [J \cdot J \cdot J \cdot J]_{jj}$	$\int_{\mathbf{q}} J_{\mathbf{q}}^4$	$6d [2d - 1] J_1^4$
(4k)	$J_{jj'} [J \cdot J^2 + J^2 \cdot J]_{jj'}$	$2 \int_{\mathbf{q}} J_{\mathbf{k} - \mathbf{q}} J_{\mathbf{q}} \int_{\mathbf{p}} J_{\mathbf{q} - \mathbf{p}} J_{\mathbf{p}}$	0
(4l)	$[J \cdot J]_{jj'}^2$	$\int_{\mathbf{q}} J_{\mathbf{k} - \mathbf{q}}^2 J_{\mathbf{q}}^2$	$16 J_1^4 \left(\frac{d^2}{4} + \frac{1}{8} \sum_{\mu=1}^d \cos(2k_{\mu}) + \sum_{\mu < \nu} \cos k_{\mu} \cos k_{\nu} \right)$
(4m)	$J_{jj'} [J \cdot J \cdot J]_{jj'}$	$\int_{\mathbf{q}} J_{\mathbf{k} - \mathbf{q}} J_{\mathbf{q}}^3$	$3 [2d - 1] J_1^3 \tilde{J}_{\mathbf{k}}$

Table VI. Geometry factors $t^{(nx)} [J]$ for Σ -diagrams of order $n = 4$. See the caption of Tab. I for remarks.

	Ising $T^{1+n}\sigma^{zz(nx)}$	TFIM $\sigma^{xx(nx)}(i\nu) _{T=0}$	Heisenberg: $T^{1+n}\sigma^{zz(nx)}(0)$	Heisenberg: $T^{1+n}\sigma^{zz(nx)}(i\nu_m \neq 0)$
(4a)	$\frac{1}{4!}b_{c,3}b_{c,5}$	$\frac{-S^2(195h^4+38h^2\nu^2+3\nu^4)}{512h^3(h^2+\nu^2)^2(9h^2+\nu^2)}$	$\frac{b_{c,1}^2}{-240}(192b_{c,1}^3+80b_{c,1}^2+20b_{c,1}+3)$	$\frac{\Delta^2b_{c,1}^2}{15}(4[30\Delta^2+1]b_{c,1}+12b_{c,1}^2+15\Delta^2+2)$
(4b)	$\frac{3}{4!}b_{c,1}^2b_{c,5}$	$\frac{S^3(447h^6+405h^4\nu^2+93h^2\nu^4+7\nu^6)}{256h^3(h^2+\nu^2)^3(9h^2+\nu^2)}$	$\frac{b_{c,1}^3}{24}(48b_{c,1}^2+12b_{c,1}+1)$	$\frac{\Delta^2b_{c,1}^3}{-3}(6b_{c,1}+30\Delta^2+1)$
(4c)	0	0	$\frac{b_{c,1}^2}{-120}(12b_{c,1}^2+6b_{c,1}+1)$	$\frac{\Delta^2b_{c,1}^2}{-15}(4[30\Delta^2+1]b_{c,1}+12b_{c,1}^2+15\Delta^2+2)$
(4d)	0	0	$\frac{b_{c,1}^3}{24}(4b_{c,1}+1)$	$\frac{\Delta^2b_{c,1}^3}{-2}$
(4e)	0	0	$\frac{b_{c,1}^3}{48}(4b_{c,1}+1)$	$\frac{\Delta^2b_{c,1}^3}{-3}(6b_{c,1}+30\Delta^2+1)$
(4f)	$\frac{6}{4!}b_{c,1}b_{c,3}^2$	$\frac{S^3(21h^2+5\nu^2)}{256h^3(h^2+\nu^2)^2}$	$b_{c,1}^3\left(b_{c,1}^2+\frac{b_{c,1}}{3}+\frac{1}{30}\right)$	$\frac{\Delta^2b_{c,1}^3}{-3}(6b_{c,1}+12\Delta^2+1)$
(4g)	$\frac{12}{4!}b_{c,1}b_{c,3}^2$	$\frac{S^3(21h^2+\nu^2)}{16h(h^2+\nu^2)^2(9h^2+\nu^2)}$	$\frac{b_{c,1}^3}{120}(144b_{c,1}^2+48b_{c,1}+5)$	$\frac{b_{c,1}^3}{3}\Delta^2(12\Delta^2+1)$
(4h)	0	0	$\frac{b_{c,1}^3}{120}$	$-6\Delta^2b_{c,1}^3$
(4i)	0	0	$\frac{b_{c,1}^3}{120}(10b_{c,1}+1)$	$\frac{b_{c,1}^3}{6}\Delta^2(24\Delta^2-1)$
(4j)	$\frac{12}{4!}b_{c,1}^3b_{c,3}$	$\frac{-5S^4(11h^2+3\nu^2)}{256h^3(h^2+\nu^2)^2}$	$\frac{b_{c,1}^4}{-6}(6b_{c,1}+1)$	$+2\Delta^2b_{c,1}^4$
(4k)	0	0	$\frac{b_{c,1}^3}{-120}$	$\frac{b_{c,1}^3}{-6}\Delta^2(24\Delta^2-1)$
(4l)	0	0	0	0
(4m)	0	0	0	$-2\Delta^2b_{c,1}^4$

Table VII. Ising model, TFIM at $T = 0$ and Heisenberg model: The lattice independent part $\sigma^{(nx)}$ for $n = 4$ for all topologies, c.f. Eq. (18). The Ising case is purely static.

[1] M. Endres, H. Bernien, A. Keesling, H. Levine, E. R. Anschuetz, A. Krajenbrink, C. Senko, V. Vuletic, M. Greiner, and M. D. Lukin, Atom-by-atom assembly of defect-free one-dimensional cold atom arrays, *Science* **354**, 1024 (2016).

[2] D. Barredo, S. de Léséleuc, V. Lienhard, T. Lahaye, and A. Browaeys, An atom-by-atom assembler of defect-free arbitrary two-dimensional atomic arrays, *Science* **354**, 1021 (2016).

[3] J. T. Barreiro, M. Müller, P. Schindler, D. Nigg, T. Monz, M. Chwalla, M. Hennrich, C. F. Roos, P. Zoller, and R. Blatt, An open-system quantum simulator with trapped ions, *Nature* **470**, 486 (2011).

[4] A. Shankar, E. A. Yuzbashyan, V. Gurarie, P. Zoller, J. J. Bollinger, and A. M. Rey, Simulating dynamical phases of chiral $p+ip$ superconductors with a trapped ion magnet, *PRX Quantum* **3**, 040324 (2022).

[5] A. Frisk Kockum, A. Miranowicz, S. De Liberato, S. Savasta, and F. Nori, Ultrastrong coupling between light and matter, *Nature Reviews Physics* **1**, 19 (2019).

[6] K. Baumann, C. Guerlin, F. Brennecke, and T. Esslinger, Dicke quantum phase transition with a superfluid gas in an optical cavity, *Nature* **464**, 1301 (2010).

[7] R. Landig, L. Hruby, N. Dogra, M. Landini, R. Mottl, T. Donner, and T. Esslinger, Quantum phases from competing short- and long-range interactions in an optical lattice, *Nature* **532**, 476 (2016).

[8] A. Browaeys and T. Lahaye, Many-Body Physics with Individually-Controlled Rydberg Atoms, *Nature Physics* **16**, 132 (2020).

[9] C. Monroe, W. C. Campbell, L.-M. Duan, Z.-X. Gong, A. V. Gorshkov, P. W. Hess, R. Islam, K. Kim, N. M. Linke, G. Pagano, P. Richerme, C. Senko, and N. Y. Yao, Programmable quantum simulations of spin systems with trapped ions, *Reviews of Modern Physics* **93**, 025001 (2021).

[10] S.-A. Guo, Y.-K. Wu, J. Ye, L. Zhang, W.-Q. Lian, R. Yao, Y. Wang, R.-Y. Yan, Y.-J. Yi, Y.-L. Xu, B.-W. Li, Y.-H. Hou, Y.-Z. Xu, W.-X. Guo, C. Zhang, B.-X. Qi, Z.-C. Zhou, L. He, and L.-M. Duan, A site-resolved two-dimensional quantum simulator with hundreds of trapped ions, *Nature* **630**, 613 (2024).

[11] W. Guerin, M. O. Araújo, and R. Kaiser, Subradiance in a large cloud of cold atoms, *Phys. Rev. Lett.* **116**, 083601 (2016).

[12] J. Rui, D. Wei, A. Rubio-Abadal, S. Hollerith, J. Zeiher, D. M. Stamper-Kurn, C. Gross, and I. Bloch, A subradiant optical mirror formed by a single structured atomic layer, *Nature* **583**, 369 (2020).

[13] P. Kongkhambut, J. Skulte, L. Mathey, J. G. Cosme, A. Hemmerich, and H. Keßler, Observation of a continuous time crystal, *Science* **377**, 670 (2022).

[14] A. Cabot, F. Carollo, and I. Lesanovsky, Continuous sensing and parameter estimation with the boundary time crystal, *Phys. Rev. Lett.* **132**, 050801 (2024).

[15] A. Auerbach, *Interacting Electrons and Quantum Magnetism*, 1994th ed. (Springer, New York, 1994).

[16] J. Larson, B. Damski, G. Morigi, and M. Lewenstein, Mott-insulator states of ultracold atoms in optical resonators, *Phys. Rev. Lett.* **100**, 050401 (2008).

[17] P. Kirton, M. M. Roses, J. Keeling, and E. G. D. Torre, Introduction to the Dicke Model: From Equilibrium to Nonequilibrium, and Vice Versa, *Adv. Quantum Technol.* **2**, 1800043 (2019).

[18] F. Mivehvar, F. Piazza, T. Donner, and H. Ritsch, Cavity QED with Quantum Gases: New Paradigms in Many-Body Physics, *Advances in Physics* **70**, 1 (2021).

[19] M. B. M. Svendsen and B. Olmos, Modified dipole-dipole interactions in the presence of a nanophotonic waveguide, *Quantum* **7**, 1091 (2023).

[20] F. Le Kien and A. Rauschenbeutel, Nanofiber-mediated chiral radiative coupling between two atoms, *Phys. Rev. A* **95**, 023838 (2017).

[21] B. Sbierski, M. Bintz, S. Chatterjee, M. Schuler, N. Y. Yao, and L. Pollet, Magnetism in the two-dimensional dipolar XY model, *Physical Review B* **109**, 144411 (2024).

[22] C. Chen, G. Bornet, M. Bintz, G. Emperauger, L. Leclerc, V. S. Liu, P. Scholl, D. Barredo, J. Hauschild, S. Chatterjee, M. Schuler, A. M. Läuchli, M. P. Zalestiel, T. Lahaye, N. Y. Yao, and A. Browaeys, Continuous symmetry breaking in a two-dimensional Rydberg array, *Nature* **616**, 691 (2023).

[23] C. Chen, G. Emperauger, G. Bornet, F. Caleca, B. Gély, M. Bintz, S. Chatterjee, V. Liu, D. Barredo, N. Y. Yao, T. Lahaye, F. Mezzacapo, T. Roscilde, and A. Browaeys, *Spectroscopy of elementary excitations from quench dynamics in a dipolar XY Rydberg simulator* (2023), arXiv:2311.11726.

[24] A. W. Sandvik, Computational Studies of Quantum Spin Systems, *AIP Conference Proceedings* **1297**, 135 (2010).

[25] A. Lohmann, H.-J. Schmidt, and J. Richter, Tenth-order high-temperature expansion for the susceptibility and the specific heat of spin- s Heisenberg models with arbitrary exchange patterns: Application to pyrochlore and kagome magnets, *Physical Review B* **89**, 014415 (2014).

[26] P. Adelhardt, J. A. Koziol, A. Langheld, and K. P. Schmidt, Monte Carlo Based Techniques for Quantum Magnets with Long-Range Interactions, *Entropy* **26**, 401 (2024).

[27] H. Bruus, K. Flensberg, H. Bruus, and K. Flensberg, *Many-Body Quantum Theory in Condensed Matter Physics: An Introduction*, Oxford Graduate Texts (Oxford University Press, Oxford, New York, 2004).

[28] R. Agra, F. van Wijland, and E. Trizac, On the free energy within the mean-field approximation, *European Journal of Physics* **27**, 407 (2006).

[29] R. Brout, Statistical Mechanical Theory of Ferromagnetism. High Density Behavior, *Physical Review* **118**, 1009 (1960).

[30] W. Metzner and D. Vollhardt, Correlated lattice fermions in $d = \infty$, *Physical Review Letters* **62**, 324 (1989).

[31] K. Hepp and E. H. Lieb, On the superradiant phase transition for molecules in a quantized radiation field: The dicke maser model, *Annals of Physics* **76**, 360 (1973).

[32] F. Carollo and I. Lesanovsky, Exactness of mean-field equations for open dicke models with an application to pattern retrieval dynamics, *Phys. Rev. Lett.* **126**, 230601 (2021).

[33] H. Kleinert and V. Schulte-frohlinde, *Critical Properties of Phi-4-Theories*, 1st ed. (World Scientific Publishing Co Pte Ltd, Singapore, 2001).

[34] S. L. Sondhi, S. M. Girvin, J. P. Carini, and D. Shashar, Continuous quantum phase transitions, *Reviews of Modern Physics* **69**, 315 (1997).

[35] V. G. Vaks, A. I. Larkin, and S. A. Pikin, Self-consistent field method for the description of phase transitions, *Soviet Physics JETP* **24**, 240 (1967).

[36] V. G. Vaks and A. I. Larkin, Spin waves and correlation functions in a ferromagnetic, *Soviet Physics JETP* **26**, 647 (1968).

[37] R. B. Stinchcombe, Thermal and magnetic properties of the transverse Ising model, *Journal of Physics C: Solid State Physics* **6**, 2507 (1973).

[38] R. B. Stinchcombe, Ising model in a transverse field. I. Basic theory, *Journal of Physics C: Solid State Physics* **6**, 2459 (1973).

[39] R. B. Stinchcombe, Ising model in a transverse field. II. Spectral functions and damping, *Journal of Physics C: Solid State Physics* **6**, 2484 (1973).

[40] Y. A. Izyumov and Y. N. Skryabin, *Statistical Mechanics of Magnetically Ordered Systems* (Consultants Bureau, New York, N.Y, 1988).

[41] J. Zhao, M. Song, Y. Qi, J. Rong, and Z. Y. Meng, Finite-temperature critical behaviors in 2D long-range quantum Heisenberg model, *npj Quantum Materials* **8**, 1 (2023).

[42] J. Gelhausen, M. Buchhold, A. Rosch, and P. Strack, Quantum-optical magnets with competing short- and long-range interactions: Rydberg-dressed spin lattice in an optical cavity, *SciPost Physics* **1**, 004 (2016).

[43] A. Schellenberger and K. P. Schmidt, (Almost) everything is a Dicke model - Mapping non-superradiant correlated light-matter systems to the exactly solvable Dicke model, *SciPost Physics Core* **7**, 038 (2024).

[44] G. Horwitz and H. B. Callen, Diagrammatic Expansion for the Ising Model with Arbitrary Spin and Range of Interaction, *Physical Review* **124**, 1757 (1961).

[45] F. Englert, Linked Cluster Expansions in the Statistical Theory of Ferromagnetism, *Physical Review* **129**, 567 (1963).

[46] R. Goll, D. Tarasevych, J. Krieg, and P. Kopietz, Spin functional renormalization group for quantum Heisenberg ferromagnets: Magnetization and magnon damping in two dimensions, *Physical Review B* **100**, 174424 (2019).

[47] J. Halbinger, B. Schneider, and B. Sbierski, Spectral representation of Matsubara n-point functions: Exact kernel functions and applications, *SciPost Physics* **15**, 183 (2023).

[48] A. M. Ferrenberg, J. Xu, and D. P. Landau, Pushing the limits of Monte Carlo simulations for the three-dimensional Ising model, *Physical Review E* **97**, 043301 (2018).

[49] P. H. Lundow and K. Markström, Critical behavior of the Ising model on the four-dimensional cubic lattice, *Physical Review E* **80**, 031104 (2009).

[50] P. Butera and M. Pernici, High-temperature expansions of the higher susceptibilities for the Ising model in general dimension d , *Physical Review E* **86**, 011139 (2012).

[51] J. Krieg and P. Kopietz, Exact renormalization group for quantum spin systems, *Physical Review B* **99**, 060403 (2019).

[52] J. Otsuki and Y. Kuramoto, Dynamical mean-field theory for quantum spin systems: Test of solutions for magnetically ordered states, *Physical Review B* **88**, 024427 (2013).

[53] Note that the lower-order non-local diagram (2b) vanishes for the Ising model.

[54] S. McKenzie, C. Domb, and D. L. Hunter, The high-temperature susceptibility of the classical Heisenberg model in four dimensions, *Journal of Physics A: Mathematical and General* **15**, 3909 (1982).

[55] J. Oitmaa and W. Zheng, Curie and Néel temperatures of quantum magnets, *Journal of Physics: Condensed Matter* **16**, 8653 (2004).

[56] H. W. J. Blöte and Y. Deng, Cluster Monte Carlo simulation of the transverse Ising model, *Physical Review E* **66**, 066110 (2002).

[57] I. V. Lukin, A. G. Sotnikov, J. M. Leamer, A. B. Magnan, and D. I. Bondar, Spectral gaps of two- and three-dimensional many-body quantum systems in the thermodynamic limit, *Physical Review Research* **6**, 023128 (2024).

[58] N. Defenu, T. Donner, T. Macrì, G. Pagano, S. Ruffo, and A. Trombettoni, Long-range interacting quantum systems, *Reviews of Modern Physics* **95**, 035002 (2023).

[59] N. D. Mermin and H. Wagner, Absence of Ferromagnetism or Antiferromagnetism in One- or Two-Dimensional Isotropic Heisenberg Models, *Physical Review Letters* **17**, 1133 (1966).

[60] Y. Zhang, L. Yu, J.-Q. Liang, G. Chen, S. Jia, and F. Nori, Quantum phases in circuit QED with a superconducting qubit array, *Scientific Reports* **4**, 4083 (2014).

[61] J. Rohn, M. Hörmann, C. Genes, and K. P. Schmidt, Ising model in a light-induced quantized transverse field, *Physical Review Research* **2**, 023131 (2020).

[62] K. Baumann, C. Guerlin, F. Brennecke, and T. Esslinger, Dicke quantum phase transition with a superfluid gas in an optical cavity, *Nature* **464**, 1301 (2010).

[63] G. Pupillo, A. Micheli, M. Boninsegni, I. Lesanovsky, and P. Zoller, Strongly correlated gases of rydberg-dressed atoms: Quantum and classical dynamics, *Phys. Rev. Lett.* **104**, 223002 (2010).

[64] M. Weber, Quantum Monte Carlo simulation of spin-boson models using wormhole updates, *Physical Review B* **105**, 165129 (2022).

[65] E. G. D. Torre, S. Diehl, M. D. Lukin, S. Sachdev, and P. Strack, Keldysh approach for nonequilibrium phase transitions in quantum optics: Beyond the Dicke model in optical cavities, *Physical Review A* **87**, 023831 (2013).

[66] D. Peter, S. Müller, S. Wessel, and H. P. Büchler, Anomalous Behavior of Spin Systems with Dipolar Interactions, *Physical Review Letters* **109**, 025303 (2012).

[67] B. Mukherjee, J. M. Hutson, and K. R. A. Hazard, *SU(N) magnetism with ultracold molecules* (2024), arXiv:2404.15957.

[68] Yu. A. Izumov, N. I. Chaschin, and V. Yu. Yushankhai, Longitudinal spin dynamics in the Heisenberg ferromagnet: Diagrammatic approach, *Physical Review B* **65**, 214425 (2002).

[69] T. Chen, A. Ghasemi, J. Zhang, L. Shi, Z. Tagay, L. Chen, E.-S. Choi, M. Jaime, M. Lee, Y. Hao, H. Cao, B. Winn, R. Zhong, X. Xu, N. P. Armitage, R. Cava, and C. Broholm, *Phase Diagram and Spectroscopic Evidence of Supersolids in Quantum Ising Magnet K2Co(SeO3)2* (2024), arXiv:2402.15869.

[70] B. Schneider and B. Sbierski, Taming spin susceptibilities in frustrated quantum magnets: Mean-field form and approximate nature of the quantum-to-classical correspondence (2024), arXiv:2407.09401.

[71] S. A. Kulagin, N. Prokof'ev, O. A. Starykh, B. Svistunov, and C. N. Varney, Bold Diagrammatic Monte Carlo Method Applied to Fermionized Frustrated Spins, *Physical Review Letters* **110**, 070601 (2013).

[72] R. Burkard *et al.*, Manuscript in preparation (2024).

[73] R. Rossi, Determinant Diagrammatic Monte Carlo in the Thermodynamic Limit, *Physical Review Letters* **119**, 045701 (2017).

[74] A. Rückriegel, D. Tarasevych, J. Krieg, and P. Kopietz, *Recursive algorithm for generating high-temperature expansions for spin systems and the chiral non-linear susceptibility* (2024), arXiv:2406.06270v1 [cond-mat].

[75] F. B. Kugler, S.-S. B. Lee, and J. von Delft, Multi-point Correlation Functions: Spectral Representation and Numerical Evaluation, *Physical Review X* **11**, 041006 (2021).